UNIVERSITY OF CALIFORNIA SAN DIEGO

Improving the processability of large-area conjugated polymer thin films for use in organic and tandem silicon/perovskite photovoltaics

A dissertation submitted in partial satisfaction of the
requirements for the degree Doctor of Philosophy

in

Chemical Engineering

by

Rory Runser

Committee in charge:

Professor Darren Lipomi, Chair
Professor David Fenning
Professor Tse Nga Ng
Professor Jon Pokorski
Professor Nathan Romero

2022

The dissertation of Rory Runser is approved, and it is acceptable in quality and form for publication on microfilm and electronically.

University of California San Diego

2022

DEDICATION

To my colleagues, friends, teammates, and family for their unwavering support.

TABLE OF CONTENTS

LIST OF ABBREVIATIONS

ALD	Atomic Layer Deposition
ARC	Anti-reflective Coating
BCP	Bathocuproine
CB	Chlorobenzene
CVD	Chemical Vapor Deposition
DIO	Diiodooctane
DIW	Deionized Water
DMF	Dimethylformamide
DMSO	Dimethylsulfoxide
EGaIn	Eutectic Gallium Indium
ETL	Electron Transport Layer
FA	Formamidinium
FAPbI3	Formamidinium Lead Iodide
FF	Fill Factor
FTO	Fluorine-doped Tin Oxide
HTL	Hole Transport Layer
ITO	Indium-doped Tin Oxide
IZO	Indium-doped Zinc Oxide
Jsc	Closed-circuit current density
LB	Langmuir-Blodgett
LMF	Light Management Foil
MA	Methylammonium
N-I-P	Negative-Intrinsic-Positive
OLED	Organic Light Emitting Diode
P3HpT	Poly-(3 heptyl thiopene)
P3HT	Poly-(3 hexyl thiopene)
PC61BM	Phenyl-C61-butyric acid methyl ester
PCE	Power Conversion Efficiency
PET	Polyethylene terephthalate
PIB	Polyisobutylene
P-I-N	Positive-Intrinsic-Negative
PL	Photoluminescence

PMMA	Poly(methyl-methacrylate)
PSC	Perovskite Solar Cell
PTAA	Poly(triaryl amine)
PTFE	Poly(tetrafluoroethylene)
PV	Photovoltaics
R2R	Roll-to-roll
SAM	Self-assembled Monolayer
SEM	Scanning Electron Microscopy
SnOx	Tin Oxide
SPD	Solid Phase Deposition
TCO	Transparent Conducting Oxide
UV-vis	Ultraviolet-Visible
Voc	Open-circuit Voltage
XRD	X-Ray Diffraction

LIST OF FIGURES

LIST OF TABLES

ACKNOWLEDGEMENTS

I would like to thank my advisor Prof. Darren J. Lipomi for all the opportunities and guidance in my research training and professional development that he has provided. His expertise in the fields of energy and conjugated polymers was essential to my research progress. I would also like to thank Prof. David P. Fenning for his guidance and mentorship on projects funded by the California Energy Commission, and for giving me the opportunity to expand my research areas to include additional next-generation photovoltaic technologies. I would also like to recognize committee chairs Profs. Jon Pokorski, Tse Nga Ng, and Nathan Romero for serving on my committee and for providing valuable feedback during my candidacy examination.

I am extremely grateful to past and present members of the Lipomi Lab. Prof. Laure Kayser, Prof. Charles Dhong, Dr. Sam Root, Dr. Cody Carpenter, Dr. Julian Ramirez, Dr. Mickey Finn, Dr. Rachel Blau, Dr. Allison Lim, Andrew Kleinschmidt, Beril Polat, Alex Chen, Guillermo Esparza, Laura Becerra, Tarek Rafeedi, Derick Ober, Kartik Choudhary, Juliana Foley, Jaden Cramlet, and Ignasi Simón all offered valuable contributions to my progress, discoveries and writing, and I feel fortunate to have worked with such wonderful and supportive colleagues.

I am equally grateful to past and present members of the Fenning lab with whom I have had the pleasure of working and collaborating during the course of my PhD. Moses Kodur, Justin Skaggs, Deniz Cakan, Yanqi Luo, Zachary Dorfman, Apoorva Gupta, Jack Palmer, Connor Dolan, Sean Dunfield, Tala Sidawi, Isabel Albelo, Eric Oberholtz, Taewoo Kim and Rishi Kumar have all helped to broaden my knowledge of perovskites, and fostered a welcoming and collegial atmosphere during my many hours spent in the Solar Energy Innovation Laboratory (SOLEIL).

I would also like to thank additional colleagues, collaborators, and friends at the UC San Diego Jacobs School of Engineering. My friends Darren Tan and Yixuan Li for their encouragement during challenging times, collaboration on first-year problem sets and exam studies, and innumerable hotpots spent discussing science. Thank you also to Dr. Hayley Hirsch,

Dr. Katy Kleinemolen, Jacob Schimelman, and Henry Hwang for welcoming me during the first year of my PhD.

Many thanks are due for staff at UC San Diego who provided both technical and logistical support during my studies. Dana Jimenez provided countless hours of support in guiding me through my first four years of study. Ji Song and Jeff Kleve continue to work tirelessly to approve laboratory purchases and on other fiscal matters in order to keep our lab running smoothly. Ryan Nicholl at Nano3 also provided invaluable technical support with AFM and SEM.

I would like to acknowledge financial support from the National Science Foundation Graduate Research Fellowship under grant no. DGE 1144086. Additional support was provided by the Air Force Office of Scientific Research (AFOSR) grant no. FA9550-19-1-0278, by the California Energy Commission (CEC) Grant Number EPC-16-050, and by a gift from the B Quest Giving Fund made to D.J.L. through Benefunder. I also acknowledge the use of facilities and instrumentation supported by the National Science Foundation through the University of California San Diego Materials Research Science and Engineering Center DMR-2011924, as well as the San Diego Nanotechnology Infrastructure (SDNI) of UCSD, a member of the National Nanotechnology Coordinated Infrastructure, which is supported by the National Science Foundation (Grant ECCS-2025752).

Chapter 2, in full, is a reprint of the material “Interfacial Drawing: Roll-to-Roll Coating of Semiconducting Polymer and Barrier Films onto Plastic Foils and Textiles” as it appears in Chemistry of Materials, by Runser, R., Root, S.E., Ober, D.E., Choudhary, K., Chen, A.X., Dhong, C., Urbina, A.D., and Lipomi, D.J., 2019, 9078–9086. The dissertation author was the first author of this paper, all authors contributed to this work.

Chapter 3, in full, is a reprint of the material “Stability of Perovskite Films Encapsulated in Single- and Multi-Layer Graphene Barriers” as it appears in ACS Applied Energy Materials, by Runser, R., Kodur, M., Skaggs, J.D., Cakan, D.N., Foley, J.B., Finn, M., Fenning, D.P., and

Lipomi, D.J., 2021, 10314–10322. The dissertation author was the first author of this paper, all authors contributed to this work.

Chapter 4, in full, is a reprint of the material “Solid Phase Deposition of Polymeric Hole Transport Layer for Conformal Coating of Monolithic 2-Terminal Perovskite/Silicon Tandem Solar Cells” which is currently under preparation for submission, by Runser, R., Esparza, G., Cramlet, J., Gupta, A., Kodur, M., Chen, A.X., Simon, I., Fenning, D.P., and Lipomi, D.J. The dissertation author was the first author of this paper, all authors contributed to this work.

VITA

2015 Bachelor of Science, Chemical Engineering, University of California Berkeley

2019 Master of Science, Chemical Engineering, University of California San Diego

2022 Doctor of Philosophy, Chemical Engineering, University of California San Diego

PUBLICATIONS

(* = authors contributed equally to the work)

1. Wangperawong, A.; Herron, S. M.; Runser, R.; Hägglund, C.; Tanskanen, J. T.; Lee, H.-B.-R.; Clemens, B. M.; Bent, S. F., Vapor transport deposition and epitaxy of orthorhombic SnS on glass and NaCl substrates. *Applied Physics Letters* **2013,** *103* (5), 052105.

2. Wills, A. W.; Michalak, D. J.; Ercius, P.; Rosenberg, E. R.; Perciano, T.; Ushizima, D.; Runser, R.; Helms, B. A., Block Copolymer Packing Limits and Interfacial Reconfigurability in the Assembly of Periodic Mesoporous Organosilicas. *Advanced Functional Materials* **2015,** *25* (26), 4120-4128.

3. Runser, R.*; Root, S. E.*; Ober, D. E.; Choudhary, K.; Chen, A. X.; Dhong, C.; Urbina, A. D.; Lipomi, D. J., Interfacial Drawing: Roll-to-Roll Coating of Semiconducting Polymer and Barrier Films onto Plastic Foils and Textiles. *Chemistry of Materials* **2019,** *31* (21), 9078-9086.

4. Keef, C. V.; Kayser, L. V.; Tronboll, S.; Carpenter, C. W.; Root, N. B.; Finn, M., 3rd; O'Connor, T. F.; Abuhamdieh, S. N.; Davies, D. M.; Runser, R.; Meng, Y. S.; Ramachandran, V. S.; Lipomi, D. J., Virtual Texture Generated using Elastomeric Conductive Block Copolymer in Wireless Multimodal Haptic Glove. *Adv Intell Syst* **2020,** *2* (4).

5. Runser, R.*; Kodur, M.*; Skaggs, J. H.; Cakan, D. N.; Foley, J. B.; Finn, M.; Fenning, D. P.; Lipomi, D. J., Stability of Perovskite Films Encapsulated in Single- and Multi-Layer Graphene Barriers. *ACS Applied Energy Materials* **2021,** *4* (9), 10314-10322.

6. Choudhary, K.; Chen, A. X.; Pitch, G. M.; Runser, R.; Urbina, A.; Dunn, T. J.; Kodur, M.; Kleinschmidt, A. T.; Wang, B. G.; Bunch, J. A.; Fenning, D. P.; Ayzner, A. L.; Lipomi, D. J., Comparison of the Mechanical Properties of a Conjugated Polymer Deposited Using Spin Coating, Interfacial Spreading, Solution Shearing, and Spray Coating. *ACS Appl Mater Interfaces* **2021,** *13* (43), 51436-51446..

7. Blau, R.; Chen, A. X.; Polat, B.; Becerra, L. L.; Runser, R.; Zamanimeymian, B.; Choudhary, K.; Lipomi, D. J., Intrinsically Stretchable Block Copolymer Based on PEDOT:PSS for Improved Performance in Bioelectronic Applications. *ACS Appl Mater Interfaces* **2022,** *14* (4), 4823-4835.

ABSTRACT OF THE DISSERTATION

Improving the processability of large-area conjugated polymer thin films for use in organic and tandem silicon/perovskite photovoltaics

by

Rory Runser

Doctor of Philosophy in Chemical Engineering

University of California San Diego, 2022

Professor Darren Lipomi, Chair

Thin films of polymers are required for a myriad of technological applications, ranging from simple protective coatings to advanced multilayer laminates for flexible electronic devices. A class of polymers called conjugated polymers is of particular interest due to their ability to transport

electronic charge while retaining mechanical deformability. These mechanical and electronic properties are easily tunable via synthetic modification of the polymer structure, resulting in a rich diversity of materials available for study. As such, conjugated polymers have been widely incorporated in next-generation thin-film photovoltaic technologies, as a layer added to improve charge transport, light absorption, or both. Nevertheless, the vast majority of studies of these materials utilize solution processing techniques (e.g. spin-coating, blade-coating, etc.) that inherently require planar substrates. This dissertation will discuss several polymer thin film processing techniques that yield large-area free-standing polymer films, which can then be coated onto a variety of flexible, textured, and non-planar surfaces. The development and characterization of a continuous, roll-to-roll deposition process is used to generate large-area organic solar cells, as well as to coat conjugated polymer films uniformly onto a textile substrate for flexible fabric-mounted PV. In addition, a batch process deposition technique will be shown for application of polymer films onto the surface of micro-pyramids, a key requirement for tandem perovskite silicon solar cells. Lastly, solar cell encapsulation techniques for extending the lifetime of perovskite solar cells will be discussed. Ultimately, such developments will help to advance the processability and performance of next-generation photovoltaic technologies.

Chapter 1. Introduction

1.1 Introduction to Solar Energy

Over the past decade, solar technologies have experienced rapid expansion and progress.[1] The cost of installed photovoltaic (PV) electricity has dropped nearly 90%, while numerous next-generation solar technologies have seen impressive rises in performance.[2] Such progress is pivotal for the expansion of installed PV capacity, which currently sits at 113 GW but is projected to require 1700 GW by 2050 in order to achieve the US' climate goals.[3]

A solar cell is a device that can convert solar energy into electric current via the photovoltaic effect. The first solar cell, fabricated by Charles Fritts in 1884, consisted of a gold-selenium heterojunction and featured a very low current output.[4] Further progress would not occur until the year 1940, when researchers at Bell labs accidentally produced a silicon wafer with a p-n junction, and noticed that current flowed through the sample when exposed to light.[5] At this point research efforts to improve device performance began in earnest, with advances in silicon processing and doping leading to increased power output. In recent decades, the performance of silicon solar cells has plateaued around 20-22% efficiency;[6] however, the cost of fabrication has dropped dramatically as increased demand has led to better economies of scale during manufacturing.[2] In addition, numerous alternate materials and architectures have also entered the R&D and manufacturing spheres, with thin-film, flexible, multi-junction, and concentrator technologies each being produced for relevant applications.[7] Nevertheless, despite the impressive progress in recent years towards expanding PV installation globally, ongoing and sustained efforts towards continued improvements in multiple PV technologies are needed in order to substantially increase solar capacity in the US and worldwide.

1.2 Introduction to Conjugated Polymers

Conjugated polymers, also known as semiconducting polymers, are a subset of polymers that possess a unique chemical structure which enables them to conduct charge.[8] Unlike traditional insulating polymers, conjugated polymers possess an alternating single- and double-bond structure along their backbone, allowing for electron delocalization and charge transfer along the polymer chain.[9] The simplest such material, polyacetylene, was discovered in 1958, but was of little practical use due to its rigidity, insolubility, and poor conductivity. Over time, however, numerous advances to the field have occurred.[10] The addition of aliphatic side chains to the monomer units renders the resulting polymers soluble in a wide range of organic solvents, enabling further processing.[11] Meanwhile, more complex monomer units, including cyclic and polycyclic aromatic structures, allow for a tunable bandgap, hole mobility, and deformability.[12] These advances have led to conjugated polymers having numerous applications that take advantage of their inherent mechanical deformability, resilience, or toughness, applications which would be challenging to fulfill with traditional inorganic semiconductors, which tend to be rigid and brittle.[13] Examples include sensors, transistors, solar cells, liquid crystals, and LEDs.[14] Furthermore, doping of the polymers, either with small molecules or blending with polymer chains containing charged side groups, can improve electron conductivity by several orders of magnitude.[15] Such conductive polymers have now widely been used as semi-transparent flexible electrodes, wearable and implantable sensors, and bio-compatible haptic feedback devices.[16] As new polymer structures are synthesized and studied, the field of conjugated polymers continues to offer an ever-broadening list of opportunities for advancement.

1.3 Organic Solar Cells

Among the many applications of conjugated polymers, perhaps none has been as revolutionary as the organic solar cell. Taking advantage of their strong optical absorbance in the visible light spectrum, as well as their electronic conductivity, conjugated polymer-based solar

cells are an active field of research—also known as Organic Photovoltaics (OPV)—that has grown rapidly over the last decade.[17] An overview of OPV architecture and operation is shown in **Figure 1.1**.

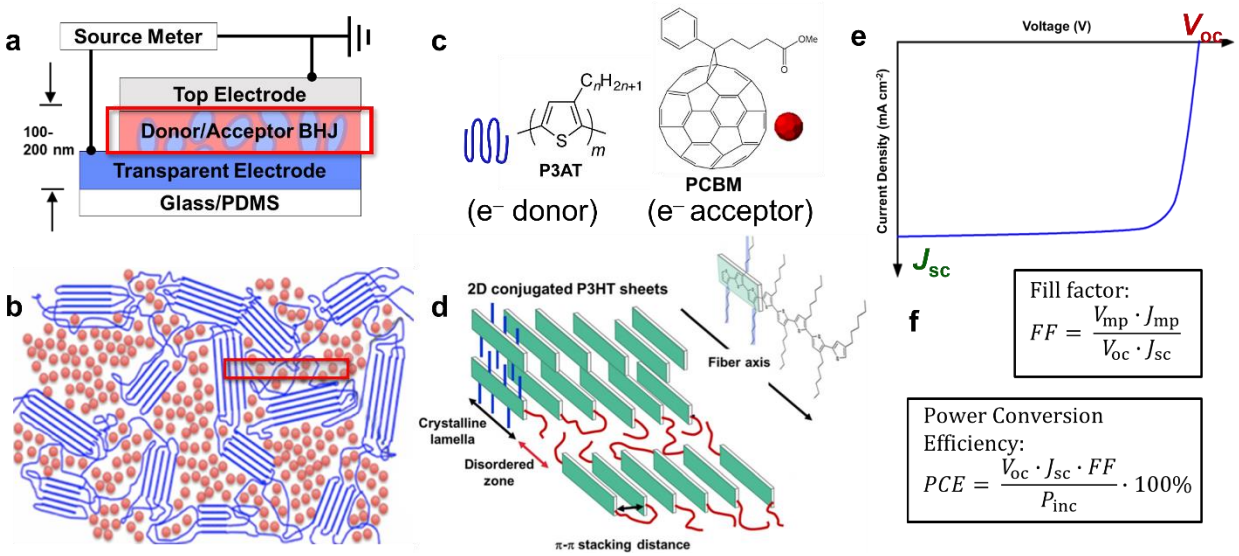

Figure 1.1 Overview of organic solar cells (a) Schematic of organic solar cell architecture. (b) Morphology of bulk heterojunction (c) Chemical structures of common donor and acceptor molecules. (d) Morphology of chain alignment within ordered regions of conjugated polymer films. (e) Representative current density-voltage (*J*-V) curve used for testing solar cell device performance (f) Equations used to calculate fill factor and power conversion efficiency.

Organic solar cells consist of a sandwich of two electrodes, surrounding an interface between an electron donating material and electron accepting material. When struck with an incident photon, an electron in the donor material is excited from the valence band to the conduction band, where it is then transferred to the acceptor material and ultimately to the adjoining electrode. Meanwhile, the residual hole travels to the opposite electrode, recombining in the attached load to complete the circuit and current flow. The solubility of these materials in organic solvents means that organic solar cells can be processed directly from solution via a number of existing commercial printing and coating techniques (e.g. blade coating, inkjet printing, etc) and at room temperature.[18,19] Furthermore, although these specialty polymers are expensive to synthesize, only a small amount of material is needed (~ 10^2 nm compared to 10^2 µm for silicon PV), and thus can be cost-competitive in terms of fabrication.[20] Still, a remaining challenge to this technology is that the

efficiencies of reported devices are lower than that of more mature technologies (the current record reported device has an efficiency of 19 %,[21] compared to 26% for silicon[22]).

The most common materials used in organic solar cells are typically a p-type conjugated polymer donor and a fullerene-based small molecule electron acceptor.[8] These materials are blended to form a bulk heterojunction, which is a highly intercalated morphology offering large interfacial areas and short diffusion lengths for charge carriers[23] (**Figure 1.1b**). While such a structure has offered a convenient pathway for research pursuits due to its adequate charge collection and extraction, alongside straightforward processing considerations, several downsides exist. Firstly, the small molecule acceptors used in BHJ blends can cause the resulting film to lose much of its elasticity and become brittle, defeating many of the purported benefits of organic solar cells.[24] Furthermore, intense focus on the BHJ structure means that other architectures which may be superior for certain material combinations may never have been explored. In recent years, some of these concerns have started to be addressed by researchers. Non-fullerene acceptors and n-type conjugated polymers have begun to replace fullerene acceptors, enabling high-performing devices without compromising mechanical compliance.[25] Novel processing techniques, including sequential deposition and orthogonal solvent use, have allowed for layering of different polymers to form various heterojunction structures apart from the BHJ.[26] Overall, there is substantial interest currently in the field of organic photovoltaics, with numerous avenues in which to pursue novel discoveries and advancement.

1.4 Conjugated Polymers for Perovskite Solar Cells

Perovskite solar cells (PSCs) are another next-generation solar technology that has recently experienced rapid progress in device performance.[27] Unlike their organic counterparts, perovskite solar cells utilize a combination of organic and inorganic compounds to form a hybrid crystal structure as an intrinsic light absorbing layer.[28] By varying the composition of the perovskite layer, the light absorbance and bandgap can be easily tuned, yielding a rich diversity of

perovskites available for researchers.[29] Whereas in an organic solar cell, where charge separation and extraction is driven by the interface between a p-type and n-type organic molecule, PSCs include charge transport layers—known as the Hole Transport Layer (HTL) and Electron Transport Layer (ETL)—that sandwich the perovskite layer. The band alignments of these layers help direct charges towards the appropriate electrodes.[30] Much like the rich diversity of perovskites that have been studied, substantial research has been undertaken on a wide array of ETL and HTL materials, which can consist of either inorganic or organic materials.[31] The HTL in particular typically consists of organic small molecules or conjugated polymers, which can form reliable and stable interactions with perovskite grains, including cross-linking that can improve device lifetime and performance.[32] Unlike in organic solar cells, where the conjugated polymer layer must be thick (>100 nm) and light-absorbing, in PSCs, the opposite is desired, specifically a thin (~10 nm) and optically transparent electronically conductive layer. These constraints result in added processing challenges that need to be addressed and overcome when considering the commercialization of PSCs, as well as PSC derivatives such as perovskite/silicon tandem solar cells. As research efforts on PSCs continues to expand, continued studies on their polymeric transport layers is key towards guaranteeing their performance and longevity.

1.5 References

(1) Green, M. A.; Hishikawa, Y.; Dunlop, E. D.; Levi, D. H.; Hohl-Ebinger, J.; Ho-Baillie, A. W. Y. Solar Cell Efficiency Tables (Version 52). *Prog. Photovoltaics Res. Appl.* **2018**, *26* (7), 427–436. https://doi.org/10.1002/pip.3040.

(2) Pillai, U. Drivers of Cost Reduction in Solar Photovoltaics. *Energy Econ.* **2015**, *50*, 286–293. https://doi.org/10.1016/j.eneco.2015.05.015.

(3) Feldman, D.; Ramasamy, V.; Fu, R.; Ramdas, A.; Desai, J.; Margolis, R. U.S. Solar Photovoltaic System and Energy Storage Cost Benchmark: Q1 2020. *Natl. Renew. Energy Lab.* **2021**, No. September, 1–120.

(4) Philip R. Wolfe. What Is Photovoltaics? *IEEE J. Photovoltaics* **2018**, 9–24.

(5) Goetzberger, A.; Hebling, C. Photovoltaic Materials, Past, Present, Future. *Sol. Energy Mater. Sol. Cells* **2000**, *62* (1), 1–19. https://doi.org/10.1016/S0927-0248(99)00131-2.

(6) Lee, Y. J.; Kim, B. S.; Ifitiquar, S. M.; Park, C.; Yi, J. Silicon Solar Cells: Past, Present and

the Future. *J. Korean Phys. Soc.* **2014**, *65* (3), 355–361. https://doi.org/10.3938/jkps.65.355.

(7) Asakura, T.; Kamiya, T.; Krausz, F.; Monemar, B.; Venghaus, H.; Weber, H.; Weinfurter, H. *Next Generation Photovoltaics*; 2012. https://doi.org/10.1887/0750309059.

(8) Root, S. E.; Savagatrup, S.; Printz, A. D.; Rodriquez, D.; Lipomi, D. J. Mechanical Properties of Organic Semiconductors for Stretchable, Highly Flexible, and Mechanically Robust Electronics. *Chem. Rev.* **2017**, *117*, 6467–6499. https://doi.org/10.1021/acs.chemrev.7b00003.

(9) Guo, X.; Baumgarten, M.; Müllen, K. Designing π-Conjugated Polymers for Organic Electronics. *Prog. Polym. Sci.* **2013**, *38* (12), 1832–1908. https://doi.org/10.1016/j.progpolymsci.2013.09.005.

(10) Rasmussen, S. C. Conjugated and Conducting Organic Polymers: The First 150 Years. *Chempluschem* **2020**, *85* (7), 1412–1429. https://doi.org/10.1002/cplu.202000325.

(11) Mei, J.; Bao, Z. Side Chain Engineering in Solution-Processable Conjugated Polymers. *Chem. Mater.* **2014**, *26* (1), 604–615. https://doi.org/10.1021/cm4020805.

(12) Hutchison, G. R.; Ratner, M. A.; Marks, T. J. Accurate Prediction of Band Gaps in Neutral Heterocyclic Conjugated Polymers. *J. Phys. Chem. A* **2002**, *106* (44), 10596–10605. https://doi.org/10.1021/jp025999m.

(13) Chen, A. X.; Kleinschmidt, A. T.; Choudhary, K.; Lipomi, D. J. Beyond Stretchability: Strength, Toughness, and Elastic Range in Semiconducting Polymers. *Chem. Mater.* **2020**, *32* (18), 7582–7601. https://doi.org/10.1021/acs.chemmater.0c03019.

(14) Reynolds, J.; Thompson, B.; Skotheim, T. *Conjugated Polymers: Properties, Processing, and Applications*; 2019.

(15) Gross, M.; Müller, D. C.; Nothofer, H. G.; Scherf, U.; Neher, D.; Bräuchle, C.; Meerholz, K. Improving the Performance of Doped π-Conjugated Polymers for Use in Organic Light-Emitting Diodes. *Nature* **2000**, *405* (6787), 661–665. https://doi.org/10.1038/35015037.

(16) Blau, R.; Chen, A. X.; Polat, B.; Becerra, L. L.; Runser, R.; Zamanimeymian, B.; Choudhary, K.; Lipomi, D. J. Intrinsically Stretchable Block Copolymer Based on PEDOT:PSS for Improved Performance in Bioelectronic Applications. *ACS Appl. Mater. Interfaces* **2022**, *14* (4), 4823–4835. https://doi.org/10.1021/acsami.1c18495.

(17) Spanggaard, H.; Krebs, F. C. A Brief History of the Development of Organic and Polymeric Photovoltaics. *Sol. Energy Mater. Sol. Cells* **2004**, *83* (2–3), 125–146. https://doi.org/10.1016/j.solmat.2004.02.021.

(18) Søndergaard, R. R.; Hösel, M.; Krebs, F. C. Roll-to-Roll Fabrication of Large Area Functional Organic Materials. *Journal of Polymer Science, Part B: Polymer Physics*. January 1, 2013, pp 16–34. https://doi.org/10.1002/polb.23192.

(19) Runser, R.; Root, S. E.; Ober, D. E.; Choudhary, K.; Chen, A. X.; Dhong, C.; Urbina, A. D.; Lipomi, D. J. Interfacial Drawing: Roll-to-Roll Coating of Semiconducting Polymer and Barrier Films onto Plastic Foils and Textiles. *Chem. Mater.* **2019**, *31* (21), 9078–9086. https://doi.org/10.1021/acs.chemmater.9b03343.

(20) Krebs, F. C.; Tromholt, T.; Jørgensen, M.; Cao, W.; Xue, J. Upscaling of Polymer Solar Cell Fabrication Using Full Roll-to-Roll Processing. *Nanoscale* **2010**, *2* (7), 2123–2144.

https://doi.org/10.1039/c4ee00260a.

(21) Zhu, L.; Zhang, M.; Xu, J.; Li, C.; Yan, J.; Zhou, G.; Zhong, W.; Hao, T.; Song, J.; Xue, X.; Zhou, Z.; Zeng, R.; Zhu, H.; Chen, C.; Mackenzie, R. C. I.; Zou, Y.; Nelson, J.; Zhang, Y.; Sun, Y. Single-Junction Organic Solar Cells with over 19% Efficiency Enabled by a Refined Double-Fibril Network Morphology. *Nat. Mater.* **2022**. https://doi.org/10.1038/s41563-022-01244-y.

(22) Ribeyron, P. J. Crystalline Silicon Solar Cells: Better than Ever. *Nat. Energy* **2017**, *2* (5), 1–2. https://doi.org/10.1038/nenergy.2017.67.

(23) Jean, R. Molecular Bulk Heterojunctions: An Emerging Approach to Organic Solar Cells. *Acc. Chem. Res.* **2009**, *42* (11), 1719–1730. https://doi.org/10.1021/ar900041b.

(24) Savagatrup, S.; Printz, A. D.; O'Connor, T. F.; Zaretski, A. V.; Rodriquez, D.; Sawyer, E. J.; Rajan, K. M.; Acosta, R. I.; Root, S. E.; Lipomi, D. J. Mechanical Degradation and Stability of Organic Solar Cells: Molecular and Microstructural Determinants. *Energy Environ. Sci.* **2015**, *8* (1), 55–80. https://doi.org/10.1039/c4ee02657h.

(25) Yan, C.; Barlow, S.; Wang, Z.; Yan, H.; Jen, A. K. Y.; Marder, S. R.; Zhan, X. Non-Fullerene Acceptors for Organic Solar Cells. *Nat. Rev. Mater.* **2018**, *3*, 1–19. https://doi.org/10.1038/natrevmats.2018.3.

(26) Ye, L.; Xiong, Y.; Yao, H.; Gadisa, A.; Zhang, H.; Li, S.; Ghasemi, M.; Balar, N.; Hunt, A.; O'Connor, B. T.; Hou, J.; Ade, H. High Performance Organic Solar Cells Processed by Blade Coating in Air from a Benign Food Additive Solution. *Chem. Mater.* **2016**, *28* (20), 7451–7458. https://doi.org/10.1021/acs.chemmater.6b03083.

(27) Lee, S. W.; Bae, S.; Kim, D.; Lee, H. S. Historical Analysis of High-Efficiency, Large-Area Solar Cells: Toward Upscaling of Perovskite Solar Cells. *Adv. Mater.* **2020**, *32* (51). https://doi.org/10.1002/adma.202002202.

(28) Mora-Seró, I. How Do Perovskite Solar Cells Work? *Joule* **2018**, *2* (4), 585–587. https://doi.org/10.1016/j.joule.2018.03.020.

(29) Ju, D.; Dang, Y.; Zhu, Z.; Liu, H.; Chueh, C. C.; Li, X.; Wang, L.; Hu, X.; Jen, A. K. Y.; Tao, X. Tunable Band Gap and Long Carrier Recombination Lifetime of Stable Mixed CH3NH3PbxSn1- XBr3 Single Crystals. *Chem. Mater.* **2018**, *30* (5), 1556–1565. https://doi.org/10.1021/acs.chemmater.7b04565.

(30) Wali, Q.; Iftikhar, F. J.; Khan, M. E.; Ullah, A.; Iqbal, Y.; Jose, R. Advances in Stability of Perovskite Solar Cells. *Org. Electron.* **2020**, *78* (February 2019), 105590. https://doi.org/10.1016/j.orgel.2019.105590.

(31) Chen, B.; Ren, N.; Li, Y.; Yan, L.; Mazumdar, S.; Zhao, Y.; Zhang, X. Insights into the Development of Monolithic Perovskite/Silicon Tandem Solar Cells. *Adv. Energy Mater.* **2022**, *12* (4), 1–20. https://doi.org/10.1002/aenm.202003628.

(32) Kim, G. W.; Choi, H.; Kim, M.; Lee, J.; Son, S. Y.; Park, T. Hole Transport Materials in Conventional Structural (n–i–p) Perovskite Solar Cells: From Past to the Future. *Adv. Energy Mater.* **2020**, *10* (8), 1–30. https://doi.org/10.1002/aenm.201903403.

Chapter 2. Interfacial Drawing: Roll-to-Roll Coating of Semiconducting Polymer and Barrier Films onto Plastic Foils and Textiles

2.1 Introduction

Thin films of polymers are required for a myriad of technological applications ranging from simple protective coatings to advanced multilayer laminates for flexible electronic devices. A major challenge associated with existing roll-to-roll (R2R) processes for manufacturing multilayer laminates of polymers is the redissolution of layers during iterative steps of deposition from solution. Some methods of addressing this challenge include transfer printing,[1–3] vacuum deposition,[4,5] and casting layers from orthogonal solvents.[6,7] While these approaches are useful for designing lab-scale devices, in most large-scale, R2R processes for thin film deposition—such as slot-die coating, blade coating, and screen printing—the material of interest does not solidify into a film until after it is deposited onto the substrate.[8] Here we introduce a R2R-compatible process, "interfacial drawing," in which a solid polymer film is drawn onto a substrate directly from a liquid meniscus at an air-water-fluoropolymer interface (Figure 2.1).

The transport processes underlying interfacial drawing are based on the phenomenon of surface-tension driven flow of organic media on water. The first investigations into interfacial spreading have been attributed to Benjamin Franklin who, in 1773, discovered that a spoonful of oil deposited onto a pond would spread out over a very large area, evidenced by the quelling of surface waves underneath.[9] A century later, Lord Rayleigh quantified this observation by determining the thickness of the resulting oil monolayer.[10] Further advances by Agnes Pockels,[11] and later Irving Langmuir and Katherine Blodgett, led to the development of the Langmuir-Blodgett (LB) trough,[12] which enabled scientists to deposit a monolayer film of organic materials onto a solid support. These advances paved the way for improved optical coatings, transparent glass, and nanoparticle thin films.[13–17]

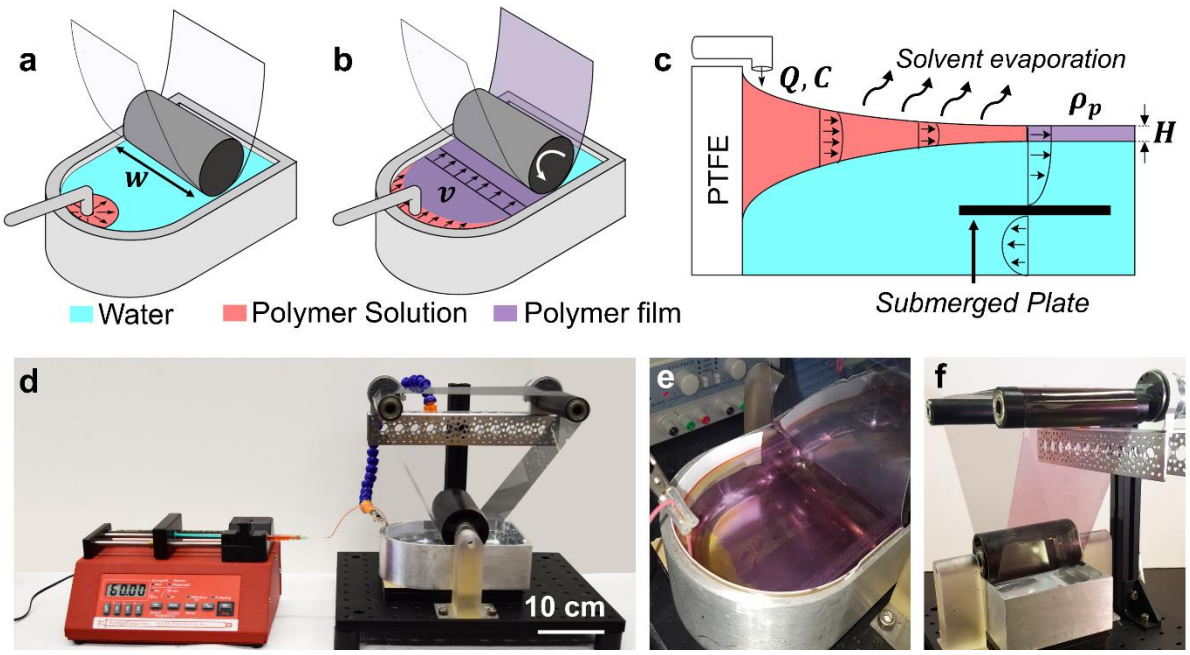

Figure 2.1 (a) Schematic drawings and photographs of the interfacial drawing process. (a) Start-up; (b) continuous operation; and (c) cross-sectional view (not to scale) of the process. All variables are defined in Table 2.1. (d) Photograph of the benchtop apparatus, including a syringe pump to control the flow of polymer solution. (e) Top-down view of polymer film on top of water bath. (f) Backside view showing polymer film coated onto a flexible polyethylene terephthalate (PET) substrate.

While much of the early research into LB films involved coatings made from amphiphilic small molecules such as fatty acids, more recent work has investigated the processing of polymer solutions using similar methods. The spreading of a polymer solution is dictated by the solution viscosity, volatility, and interfacial surface tension between the supporting liquid (typically water) and the organic solvent[18]. This natural process can yield ultra-thin (~10–80 nm) polymeric films, which have a variety of applications.[19–21] For example, recent work by Noh *et al*. has applied this method to fabricate semiconducting polymer films, and showed that the process could yield organic solar cells with improved efficiencies compared to devices fabricated by spin-coating.[22] The spontaneous nature of the solvent spreading on water also enables the generation of large-area polymeric thin films.[23] This observation motivated us to convert this batch process into a continuous, roll-to-roll (R2R) process, which would enable the formation of much larger films at a faster rate.[24] The resulting process can generate free-standing polymer films of >1 m in length with our benchtop setup.

Interfacial drawing provides an opportunity for producing large-area multilayer polymer thin films processed from the same (or similar) solvents, which could enable the fabrication of new architectures for OLEDs,[25] organic solar cells,[26] and reflective birefringent optics.[27] Additionally, the ability of interfacial drawing to coat uniform, ultra-thin (10–20 nm) polymer films (which is often difficult to achieve with other coating techniques[8]) would be beneficial to a number of fields, including sensors,[17] anti-reflection coatings,[12] and biomedical devices.[28] The ability to observe the film quality prior to deposition to the desired substrate would also be advantageous for quality control purposes in a manufacturing setting. Furthermore, interfacial drawing allows for the use of unusual and irregular substrates, as a pre-solidified film can be adhered onto the surface, rather than drying non-uniformly in pores and gaps. This capability could be of interest for developing conductive fabrics,[29–33] wearable optoelectronic devices,[34–36] or textiles with barrier coatings. In this report, we investigate in detail the operating principles behind interfacial drawing and characterize the mechanical and optoelectronic properties of the resulting films.

Table 2.1 Process variables and materials properties. Spreading coefficients were calculated from interfacial surface energies.

Parameter	Variable	Range of values	Units
Film thickness	H	10–100	nm
Width of trough	w	10	cm
Velocity	v	2–6	mm s^{-1}
Solution pump rate	Q	20–100	μL min^{-1}
Solution concentration	C	5–40	mg mL^{-1}
Polymer density (solid)	ρ_p	1.1	g cm^{-3}
Polymer solution viscosity	μ_s	1–10	MPa s
Polymer solution density	ρ_s	1.1–1.5	g cm^{-3}
Evaporative mass transfer coefficient	K_{evap}	7.75×10^{-6}	cm s^{-1}
Spreading coefficient	S	-4.2–12.1	—

2.2 Process Design

2.2.1 Design of Benchtop Apparatus

Interfacial drawing generates a uniform polymer thin film by leveraging the spontaneous spreading and drying process of a polymer solution deposited at an air-water-fluoropolymer interface (Figure 2.1a). When the solidified edge of the film is drawn onto a flexible or textile substrate, the liquid meniscus continues to spread and solidify in a continuous process (Figure 2.1b-c). Photographs of our custom-designed benchtop apparatus are shown in Figure 2.1d-f. Briefly, we custom-milled a 10 cm-wide trough in an aluminum block to serve as the water bath. (We previously found that a 3D-printed, plastic trough absorbed solvent and became difficult to clean between trials.) A trough having a semicircular edge on the end where the solution was injected was found to be preferable to a rectangular trough, as the curvature eliminated corners that became the sites of tearing the polymer film. We placed a strip of adhesive-coated polytetrafluoroethylene (PTFE) along the curved edge, to encourage the formation of a polymer

solution meniscus at the PTFE-water interface. A thin plate was submerged in the center of the trough to promote a circulatory flow within the water bath, which helped reduce eddies and velocity variations on the surface of the water bath. The roll-to-roll mechanism was constructed with 3D-printed rollers which supported a ~0.5 m loop of flexible polyethylene terephthalate (PET). The rollers were operated by DC gear motors which were connected to a power supply with a variable voltage output—which controlled the drawing velocity. The apparatus was partially shielded from external sources of vibration by supporting it on a platform with dampening rubber feet. Fumes from the chlorinated solvents were suctioned from above the process using a maneuverable exhaust snorkel.

2.2.2 Choice of Polymer Solution

2.2.2.1 Choice of Solvent

While interfacial drawing is theoretically compatible with any polymer-solvent system with a positive spreading parameter, we limited our studies to solutions prepared in chlorobenzene—a common solvent for dissolving polymeric materials, which also has a favorable spreading parameter. Other solvents were considered, but not used.

2.2.2.2 Choice of Polymers

Interfacial drawing is best suited for mechanically robust polymers which are resistant to tearing during the drawing process. For this study, semiconducting polymers were chosen as a model system because (i) their applications are exclusively limited to thin film geometries, (ii) they exhibit a wide range of mechanical properties,[37] and (iii) they strongly absorb visible light—thus they exhibit abrupt color change upon solidification, [38] and film thickness can be linearly correlated to UV-Vis absorption for rapid optical measurement of thickness on flexible substrates. Nevertheless, this process is not limited to optically active polymers, and we also successfully fabricated films of conventional transparent plastics.

The structures of the materials used in this study are given in Figure 2.2a. In order to investigate the utility of interfacial drawing for materials with various microstructures and mechanical properties, we began our study using PTB7, a predominantly amorphous polymer,[39] and P3HT, a semicrystalline polymer—which is often considered a model material in semiconducting polymer research.[40] Large-area (10 cm × 20 cm) thin films of these materials made using interfacial drawing and coated onto a flexible PET substrate are shown in Figure 2.2b-c. We did note some tears and variations in thickness within the outer 2 cm edges of these films, likely due to uneven circulation of the water along the edges of the trough. The middle regions of the films (indicated by the dashed lines in Figure 2b-d), however, were uniform, with variations of ±3–6 nm from the average. Additionally, we sometimes observed wrinkling in P3HT films, likely due to the glassy nature of P3HT at room temperature (in contrast to PTB7, which did not exhibit wrinkling). The addition of a plasticizer, such as 1-8 diiodooctane (DIO, often used as an additive to improve the performance of organic solar cells), serves to eliminate these wrinkles from P3HT films.

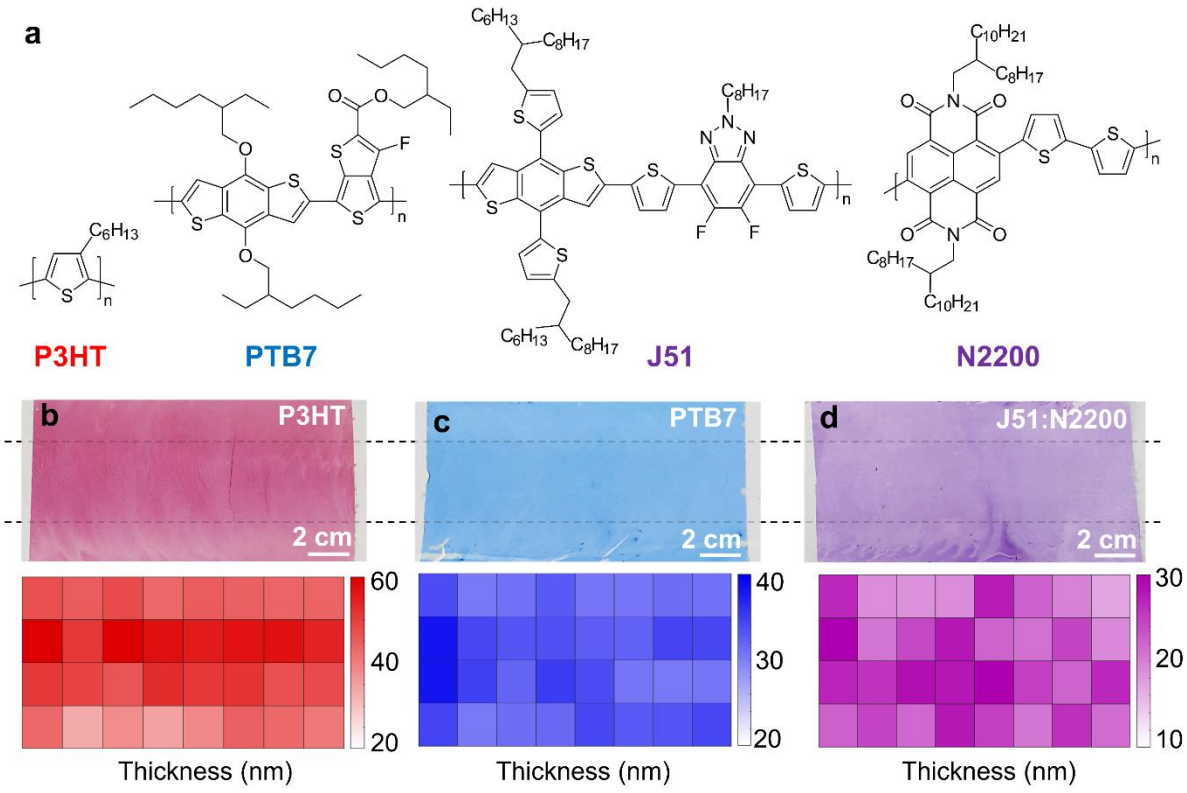

Figure 2.2 Semiconducting polymer films produced by interfacial drawing: chemical structures, photographs, and thickness maps. (a) Chemical structures of polymers used. Refer to Experimental Methods for systematic names. Films with dimensions of 10 cm × 20 cm produced using interfacial drawing, and corresponding thickness maps obtained from UV-Vis absorption intensity, indicating the variation in thickness for (b) P3HT, (c) PTB7, and (d) J51:N2200. Each square in the heatmaps corresponds to an area of 2.5 cm × 2.5 cm. The central region of the films (denoted by the dashed lines) was found to be of a more uniform thickness than the outside edges. For these films, Q = 40 μL min^{-1}, v = 3 mm s^{-1}, and C = 20 mg mL^{-1} for P3HT and PTB7, and C = 12 mg mL^{-1} for J51:N2200.

To demonstrate the utility of interfacial drawing for the fabrication of functional organic electronic devices, we selected a binary mixture of two polymers, J51:N2200 (Figure 2.2d). All-polymer blends often possess improved mechanical resilience compared to polymer:fullerene blends,[41] and this particular blend has previously been shown to yield high-efficiency solar cells.[42] We also attempted to combine P3HT and PTB7 with the methonofullerene $PC_{61}BM$ to make a bulk heterojunction organic solar cell.[43] However, these blends yielded films that cracked upon solidification, which was not surprising given the embrittling effect of fullerenes.[37]

2.3 Results and Discussion

2.3.1 Characterization of Process Variables

2.3.1.1 Relevant Process Variables

When a polymer solution is initially injected at the water-air-PTFE interface at pump rate, Q, it spreads in two directions: (i) circumferentially to form a liquid meniscus along the semicircular interface, and (ii) onto the surface of the water to form a thin liquid film, which dries rapidly and solidifies. In theory, the characteristic thickness, H, of the dried film depends upon the surface tension, viscosity, and mass transfer coefficient of the polymer solution, all of which, in turn, depend upon the polymer-solvent system employed, and the initial concentration of the polymer, C. When the solidified edge of the film is drawn by the roller onto the substrate at a linear velocity, v, liquid from the meniscus spreads and dries to replenish the solid film with a resulting thickness which should be inversely dependent upon velocity at which it is drawn. A series of pilot experiments showed that, for a trough with width, w = 10 cm, the process operated viably for Q ~ 10 μL min^{-1}, v ~ 1 mm s^{-1}, and C ~ 10 mg mL^{-1} and that variations in the concentration of the polymer solution resulted in the most pronounced changes in film thickness.

2.3.1.2 Effect of Polymer Concentration

To assess the range of film thickness attainable by modulating the initial polymer concentration, we chose a fixed Q = 40 μL min^{-1}, and v = 3 mm s^{-1} and ran a set of trials in which the concentration was incrementally increased from 5 to 40 mg mL^{-1}. As shown in Figure 2.3a-b, we observed a linear correlation between film thickness and concentration of polymer for all three polymer solutions tested. Given similarities in surface tension, viscosity, and evaporative mass transfer coefficient of these three chlorobenzene-polymer solutions, it is not surprising that they all exhibited similar slopes relating concentration to thickness. For the solutions tested, the minimum thickness attainable was between 5–10 nm for a concentration of 5 mg mL^{-1}. Below this

concentration, the films did not exhibit sufficient mechanical robustness to be pulled by the roller without tearing. The maximum thickness attainable ranged from 30 nm for the J51:N2200 blend to 80 nm for P3HT. The P3HT solution was capable of spreading reliably up to a viscosity of 10 MPa s at 40 mg mL^{-1}, while the J51:N2200 blend exhibited non-Newtonian gel-like behavior, which prevented reliable spreading at the same concentration.

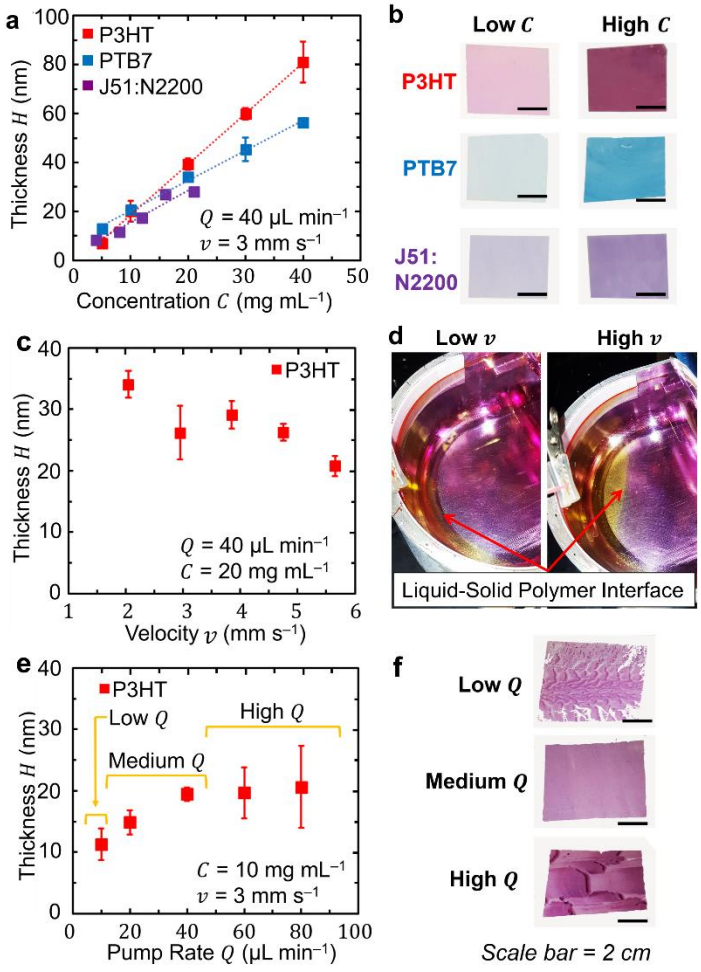

Figure 2.3 Process Characterization. (a) Plot showing the dependence of thickness on solution concentration. (b) Photos of samples made from low and high concentrations. (c) Plot showing dependence of thickness on drawing velocity. (d) Top-down photograph process showing the effect of drawing velocity on the boundary between the liquid solution (orange) and solid polymer (purple). (e) Plot showing dependence of thickness on pump rate. (f) Photos of samples made from three regimes of pump rates.

2.3.1.3 Effect of Drawing Velocity

The maximum rate for producing a film by interfacial drawing is limited by the linear velocity of the roller. To investigate the effect of this critical manufacturing parameter, we selected the

mid-range concentration of P3HT (20 mg mL^{-1}), fixed the flowrate at 40 mg mL^{-1} and incrementally varied the drawing velocity from 2–6 mm s^{-1}. As shown in Figure 2.3c, we observed that the thickness decreased as the film was drawn at a faster rate. Moreover, we observed that increasing v caused the liquid-solid polymer interface on the water bath surface to be pulled further away from the wall (Figure 2.3d). Importantly, the system remained operable until the liquid-solid boundary came in contact with the roller, suggesting that interfacial drawing could be scaled up to a larger system with faster operating speeds if it were designed with the appropriate water bath geometry (i.e. sufficient distance between the meniscus and the substrate rollers).

2.3.1.4 Effect of Pump Rate

The final parameter that was varied in our initial characterization of the system was the volumetric pump rate of polymer solution, *Q* (Figure 2.3e-f). We observed three regimes of film solidification behavior: at low values of Q (<5 µL min^{-1}), there was extensive film tearing due to an insufficient quantity polymer solution being supplied to the system; for high values of Q (>40 µL min^{-1}) films exhibited uneven solidification patterns; and in the intermediate regime, we observed uniform films with H proportional to *Q*. It can be expected that the intermediate regime of *Q* corresponds to steady-state conditions.

2.3.1.5 Steady-State Analysis

A mass balance applied to the solid polymer in the process yields the following relation:

$$C\frac{dV_m}{dt} = \left[\frac{10^{-3}\ mL}{\mu L}\right] QC - \left[\frac{6\times 10^{-4}\ s\cdot mg\cdot cm^2}{min\cdot g\cdot nm\cdot mm}\right] v\rho_p wH \qquad (1)$$

Where V_m (mL min^{-1}) is the volume of solution in the meniscus, t (min) is the time, and ρ_p (g cm^{-3}) is the density of the polymer film—which we assume to be constant and equal to 1.1 g cm^{-3}, due to experimental difficulties with the measurement of this quantity for polymer thin films. The pre-factors in equation (1) allowed us to directly input variables with the units listed in Table 2.1.

Applying equation (1) to the previously described process characterization experiments allows for the approximate quantitative characterization of the accumulation of polymer solution in the meniscus during the runs, *a posteriori*. In general, this analysis showed that the process could reliably produce uniform films under steady state conditions or in a state of accumulation.

2.3.1.6 Process Design Strategy

The process characterization experiments show that, in lieu of a predictive transport model describing the physics of the process, an iterative empirical approach can be applied to design a reliable process operating at or near steady state conditions. To coat a given polymer solution to a desired thickness, the following strategy can be applied: (i) characterize the range of thicknesses accessible via modulation of the concentration of the polymer solution, (ii) choose the concentration that will yield the desired thickness, (iii) find the maximum drawing velocity for the chosen concentration, and (iv) apply equation (1) to solve for the solution pump rate that will yield approximately steady state conditions. If the process is designed appropriately, it can be used to coat a film of consistent and desired thickness for a long duration of time. Since our benchtop setup was limited to a 0.5 m loop of PET, we demonstrated this consistency by measuring the thickness of the film after each incremental layer was added. As can be seen in Figure 2.4, by choosing the correct steady-state operating conditions, we were able to produce a film of consistent and desired thickness, over a timescale of >15 min. Further studies into the effects of surface tension, viscosity, and mass transfer coefficient of the polymer solution on the characteristic thickness of the polymer film could yield a deeper understanding of the physical

processes underlying the spreading and drying phenomena. Such knowledge could help develop a theoretical model to predict the final film thickness *a priori*.

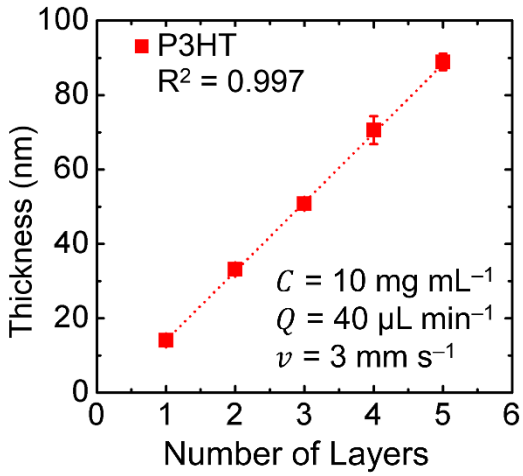

Figure 2.4 Consistency of film thickness over time. Each successive layer of P3HT is of the same thickness, over a length of 50 cm between each layer, showing that the process is operating under steady-state conditions.

2.3.1.7 Termination of Process

In all cases, the solid floating polymer films would eventually tear on the surface of the water bath or lose cohesion with the bilayer meniscus. Both of these modes of failure were initiated by vibrations, airflow, or other external disruptions from the laboratory that could in principle be mitigated by further isolating the apparatus and improving the construction. After film fracture, it was initially difficult regenerate a solid film, as the injected polymer solution accumulated only along the PTFE walls of the water bath, rather than continuing to spread. We found that the water bath had a higher contact angle on the PTFE once the solution stopped spreading (115° vs 109° for DI water), indicating that the surface energy between the water and air had decreased. Given that the spreading coefficient of chlorobenzene is already close to zero, such a small change in surface energy could easily cause the spreading parameter of the polymer solution to shift from positive to negative, inhibiting subsequent spreading. Thus, while physical disruptions such as vibrations were responsible for causing the spreading of the polymer solution

to cease, chemical contamination of the water bath prevented the subsequent restart of the process. However, after several more minutes, the spreading process would often restart spontaneously, likely due to surface contamination becoming dissipated into the water bath bulk. Working with higher purity starting materials—or finding a way to continually replenish the water bath—could likely improve the long-term stability of the system.

2.3.2 Mechanical Properties of Films from Interfacial Drawing

2.3.2.1 Elastic Modulus

Our laboratory has a specific interest in the mechanical properties of semiconducting polymers for robust and stretchable devices for energy and healthcare.[37] The elastic moduli and fracture strain of P3HT, PTB7, and J51:N2200 were measured using a film-on-water uniaxial tensile test. Figure 2.5a compares the moduli of films of these three materials prepared by spin-coating and interfacial drawing. All three of our materials exhibited a lower elastic modulus when prepared via interfacial drawing versus spin-coating. We attribute this improved compliance to the more rapid rate of drying in interfacial drawing, which occurs over a timescale of seconds, compared to several minutes for spin-coating.[22] Previous modelling work by our group and others has suggested that a faster rate of solidification results in an increase in void space within the polymer film, and thus a decrease in modulus.[44,45] In many cases, it is desirable to affect the mechanical properties of materials by way of processing, as opposed to by making changes to the molecular weight or the chemical structure. For example, decreased elastic modulus can be desirable for applications in wearable “epidermal electronics,” as the modulus of the device can more closely match the modulus of skin, and thus be “invisible” to the user.[46]

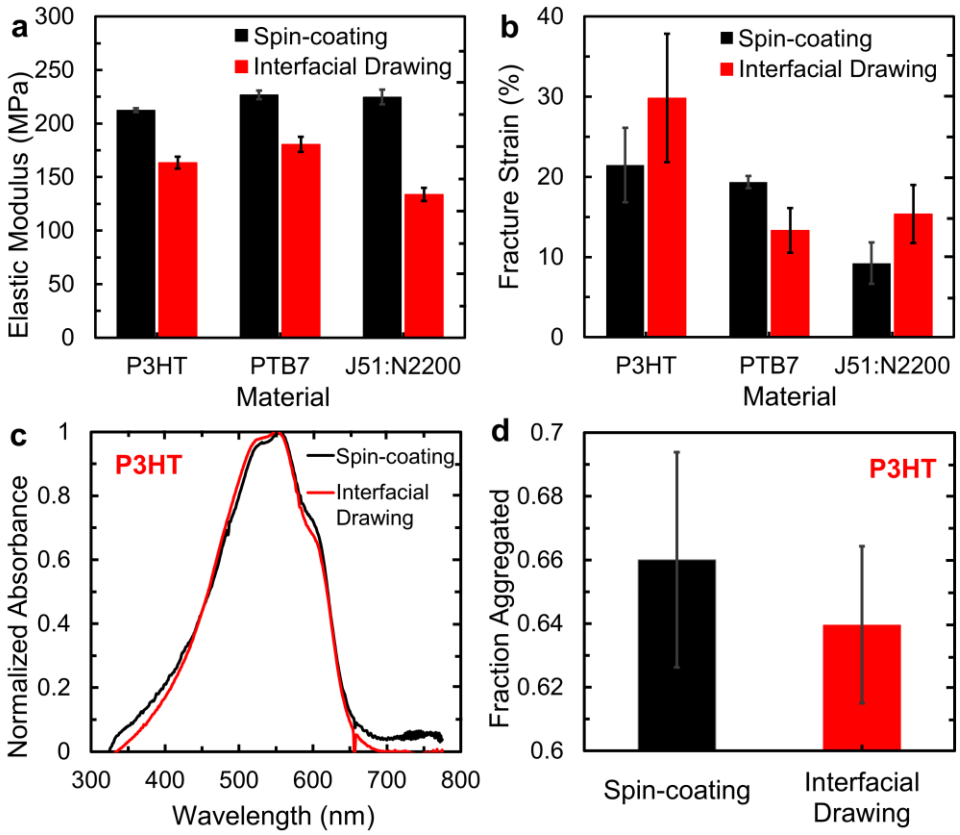

Figure 2.5 Mechanical properties of films generated from interfacial drawing and spin-coating, comparing (a) elastic modulus, and (b) fracture strain for P3HT, PTB7, and J51:N2200. (c) Absorbance vs wavelength UV-Vis spectra (normalized to the 0-1 transition at 551 nm), and (d) H-aggregate analysis, for representative P3HT samples prepared by spin-coating and interfacial drawing.

2.3.2.2 Extensibility

A high extensibility is desirable for flexible or stretchable devices. As shown in Figure 2.5b, P3HT and J51:N2200 exhibited an increased strain at fracture when prepared by spin-coating, whereas for PTB7 the extensibility was reduced. We attribute these findings to the semicrystalline nature of P3HT,[47] J51,[42] and N2200,[41] in contrast to the predominantly amorphous structure of PTB7.[39] The rapid drying rate in interfacial drawing results in a decrease in aggregation in semicrystalline films compared to spin-coating, which in turn allows for greater extensibility.[45] This observation is supported by the UV-vis spectra and H-aggregate analysis[48] of our P3HT films (Figure 2.5c-d). In films from interfacial drawing, the 0-0 transition at 606 nm is reduced, while

there is an increase in the region associated with absorption of the amorphous fraction between 450 and 500 nm, indicating decreased aggregated fraction.[49] In contrast, since PTB7 has few ordered domains to begin with, we surmise that the rapid drying rate found in interfacial drawing does not produce the same effect. Instead, the amorphous chains have less time to form entanglements, resulting in decreased extensibility compared to spin-coating.[44]

2.3.3 Coating Polymer Films onto Textile Substrates

Solution processing of polymer films onto porous, uneven, or textile substrates is inherently challenging due to uneven film morphology that results upon solidification of films. Figure 2.6a shows the effect of spin-coating a polymer film onto a fabric substrate. As the polymer solution permeates into the weave of the material, individual fibers become coated with the desired polymer, leaving gaps between fiber bundles. For some applications, this uneven morphology may be preferred, such as in the fabrication of conductive fabrics for heating applications.[32,50] In other cases, such as the application of a polymer film to a porous substrate in order to reduce its permeability in a controlled manner, it is desirable to adhere a cohesive polymer film with a uniform thickness. Figure 2.6b-c shows how polymer films can be coated onto (rather than impregnated into) the surface of a fabric using interfacial drawing. This method was successful with fabrics with a narrow spacing, such as ripstop silnylon fabric (Figure 2.6b) as well as those with a wide spacing between fibers, such as a silver-coated conductive nylon textile (Figure 2.6c). The brightly colored materials shown in Figure 2.6a-c were chosen to aid visualization of the resultant polymer film structure when using textile substrates with interfacial drawing. PMMA is better suited for coating a fabric to render it impermeable to air or water. We coated two layers of PMMA onto a piece of Ripstop silnylon tarp and measured its permeability to air using a custom-designed isochoric gas permeability apparatus, shown in Figure 2.6d. After the system is placed under a static vacuum of < 0.1 torr, one side is exposed to atmospheric

pressure, causing the pressure on the vacuum side to slowly increase. As is shown in Figure 2.6e, the PMMA acted as a barrier, reducing gas permeability by several orders of magnitude.

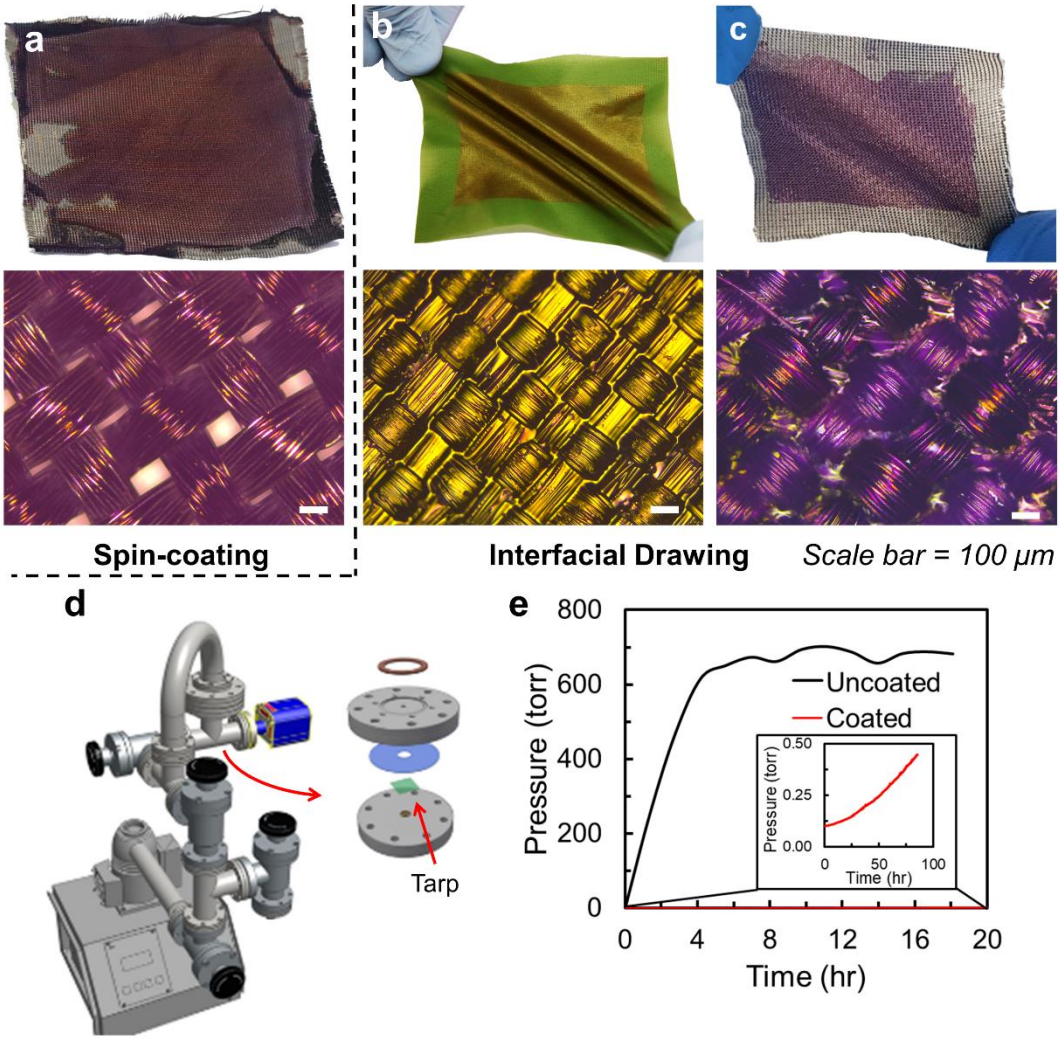

Figure 2.6 Interfacial drawing with textile substrates. (a) Spin-coating J51:N2200 onto silver nylon tarp. (b) A single layer of P3HT (~40 nm) coated onto Ripstop silnylon tarp, and (c) J51:N2200 (~30 nm) coated onto silver nylon tarp, using interfacial drawing. (d) Schematic of isochoric gas permeability apparatus, used to measure air permeability of fabrics and barrier films. (e) Pressure vs time plots for uncoated Ripstop silnylon tarp, and tarp coated with PMMA via interfacial drawing.

2.3.4 Flexible Organic Solar Cells

In order to demonstrate the capability of interfacial drawing for producing functioning organic electronic devices, we fabricated flexible organic solar cells using indium-doped tin oxide (ITO)/PET substrates and an active layer of J51:N2200. Achieving an optimal active layer

thickness of 120 nm, as reported by Gao, *et al*,[42] required coating the substrates with four successive layers of 30 nm-thick polymer films. A representative J-V plot for our solar cells, as well as for control devices fabricated via spin-coating, is shown in Figure 2.7, with tabulated solar cell performance metrics given in Table 2.2. While previous work on fabricating organic solar cells from solution-spread (non-R2R) polymer thin films reported an improved power conversion efficiency compared to spin-coating,[22] we observed a decrease in efficiency, from 2.54% to 1.71%. This difference is a result of a decrease in current density in our devices produced by interfacial drawing, along with a small decrease in fill factor. We attribute this reduced performance to interruption in charge transport between discrete layers of J51:N2200 films, and possible contamination by water. We attempted to increase the cohesion between successively deposited layers by thermal annealing; however, this action caused the efficiency to further decrease, likely due to unfavorable phase separation between the donor and acceptor material. We note that these solar cells were otherwise unoptimized. We included the result as an example of the ability of interfacial drawing to generate functional semiconducting devices, despite conventional wisdom that suggests that semiconducting polymers are easily degraded by oxygen and water.[51,52] We nevertheless believe that further optimization could substantially increase the efficiency of solar cells produced via interfacial drawing. Further investigations into a wider array of donor and acceptor materials would likely reveal a materials system which is better suited for high-efficiency flexible devices and will be the area of focus for future studies by our group.

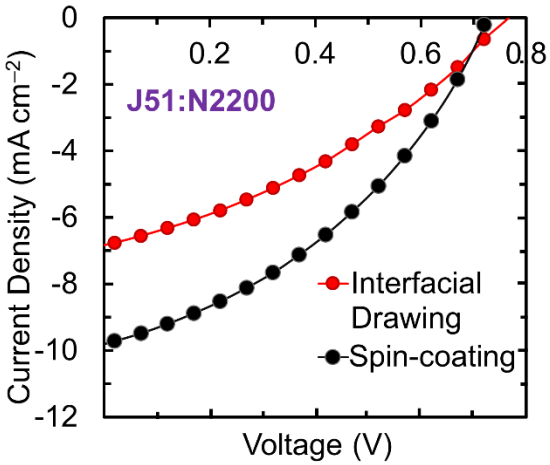

Figure 2.7 Flexible organic solar cells. Representative current density-voltage plots for solar cells fabricated using interfacial drawing and spin-coating. The full device architecture was PET/ITO/PEDOT:PSS (10 nm)/J51:N2200 (120 nm)/EGaIn.

Table 2.2 Performance metrics for flexible J51:N2200 organic solar cells on ITO/PET substrates, comparing devices prepared by interfacial drawing and by spin-coating. Average and standard deviations are given for n = 5 devices, with champion values given in parentheses.

	V_{oc} (V)	J_{sc} (mA cm^{-2})	FF	PCE (%)
Spin-coating	0.68 ± 0.05 (0.72)	10.04 ± 0.42 (10.55)	0.38 ± 0.01 (0.39)	2.54 ± 0.18 (2.75)
Interfacial Drawing	0.78 ± 0.01 (0.79)	6.31 ± 0.55 (6.83)	0.35 ± 0.01 (0.36)	1.71 ± 0.15 (1.81)

2.4 Conclusion

We introduced a new R2R process—"interfacial drawing"—for coating arbitrary substrates with solid polymer thin films supported by the surface tension of water. Experimental results show that the film thickness can be precisely controlled in the range of 10-80 nm by empirical tuning the concentration of the polymer solution as well as the drawing velocity and input flowrate of the polymer solution. We determined that, in comparison to spin-coated films, interfacial drawing yields films with a reduced elastic modulus and an increased extensibility (for semicrystalline materials), which are often desirable mechanical properties for stretchable and flexible devices. Finally, we demonstrated the utility of interfacial drawing by successfully fabricating flexible organic solar cells, and by coating polymer films onto textiles for use as fabric-mounted devices

and barriers. Future optimization of interfacial drawing will involve developing a detailed theoretical model of the transport process to circumvent the empirical strategy currently employed for designing the process. Furthermore, improved isolation of the apparatus from external vibrations, as well as scaling up the process to a larger water bath should allow for the faster coating of more uniform films over larger areas. This process should be of interest to organic materials chemists aiming to develop novel architectures of biosensors, solar cells, and wearable electronics, as well as engineers seeking new roll-to-roll processing techniques for fabricating large-area polymer thin films.

Chapter 2, in full, is a reprint of the material “Interfacial Drawing: Roll-to-Roll Coating of Semiconducting Polymer and Barrier Films onto Plastic Foils and Textiles” as it appears in Chemistry of Materials, by Runser, R., Root, S.E., Ober, D.E., Choudhary, K., Chen, A.X., Dhong, C., Urbina, A.D., and Lipomi, D.J., 2019, 9078–9086. The dissertation author was the first author of this paper, all authors contributed to this work.

2.5 References

1. We Yim, B. K.; Zheng, Z.; Liang, Z.; Friend, R. H.; Huck, W. T. S.; Kim, J. Efficient Conjugated-Polymer Optoelectronic Devices Fabricated by Thin-Film Transfer-Printing Technique. *Adv. Funct. Mater.* **2008**, *18*, 1012–1019. https://doi.org/10.1002/adfm.200701321.

2. Tada, A. Tayloring Organic Hbilayer Polymer Photovoltaic Devices. *Nat. Mater.* **2011**, *10* (6), 450–455. https://doi.org/10.1038/nmat3026.

3. O’Connor, T. F.; Zaretski, A. V.; Shiravi, B. A.; Savagatrup, S.; Printz, A. D.; Diaz, M. I.; Lipomi, D. J. Stretching and Conformal Bonding of Organic Solar Cells to Hemispherical Surfaces. *Energy Environ. Sci.* **2014**, *7*, 370–378. https://doi.org/10.1039/c3ee42898b.

4. P. Peumans, S. R. F. Very-High-Efficiency Double-Heterostructure Copper Phthalocyanine/C60 Photovoltaic Cells. *Appl. Phys. Lett.* **2001**, *76* (1), 126–128. https://doi.org/10.1063/1.1384001.

5. Torres, T.; Cheyns, D. Energy Level Tuning of Non-Fullerene Acceptors in Organic Solar Cells. *J. Am. Chem. Soc.* **2015**, *137*, 8991–8997. https://doi.org/10.1021/jacs.5b02808.

6. Aguirre, J. C.; Hawks, S. A.; Ferreira, A. S.; Yee, P.; Subramaniyan, S.; Jenekhe, S. A.; Tolbert, S. H.; Schwartz, B. J. Sequential Processing for Organic Photovoltaics : Design Rules for Morphology Control by Tailored Semi-Orthogonal Solvent Blends. *Adv. Energy Mater.* **2015**, *5*, 1–11. https://doi.org/10.1002/aenm.201402020.

7. Ye, L.; Xiong, Y.; Chen, Z.; Zhang, Q.; Fei, Z.; Henry, R.; Heeney, M.; O'Connor, B. T.; You, W.; Ade, H. Sequential Deposition of Organic Films with Eco-Compatible Solvents Improves Performance and Enables Over 12%-Efficiency Nonfullerene Solar Cells. *Adv. Mater.* **2019**, *1808153*, 1808153. https://doi.org/10.1002/adma.201808153.

8. Søndergaard, R. R.; Hösel, M.; Krebs, F. C. Roll-to-Roll Fabrication of Large Area Functional Organic Materials. *J. Polym. Sci. Part B Polym. Phys.* **2013**, *51*, 16–34. https://doi.org/10.1002/polb.23192.

9. Behroozi, P.; Cordray, K.; Griffin, W.; Behroozi, F. The Calming Effect of Oil on Water. *Am. J. Phys.* **1889**, *75* (5), 407–414. https://doi.org/10.1119/1.2710482.

10. Rayleigh, Lord. Measurements of the Amount of Oil Necessary in Order to Check the Motions of Camphor upon Water. *Proc. R. Soc. London* **1869**, *47*, 364–367.

11. Pockels, A. Understanding Solvent Spreading for Langmuir Deposition of Nanomaterial Films: A Hansen Solubility Parameter Approach. *Nature* **1893**, *48* (1233), 152–154. https://doi.org/10.1021/acs.langmuir.7b03867.

12. Roberts, G. G. An Applied Science Perspective of Langmuir- Blodgett Films. *Adv. Phys.* **1985**, *34* (4), 475–512. https://doi.org/10.1080/00018738500101801.

13. Hickel, W.; Duda, G.; Jurich, M.; Krohl, T.; Rochford, K.; Stegeman, G. I.; Swalen, J. D.; Wegner, G.; Knoll, W. Optical Waveguides from Novel Polymeric Langmuir-Blodgett Multilayer Assemblies. *Langmuir* **1990**, *6*, 1403–1407. https://doi.org/10.1021/la00098a014.

14. Paloheimo, J.; Pal, A. J.; Stubb, H. Langmuir-Blodgett Light-Emitting Diodes of Poly (3-Hexylthiophene) : Electro-Optical Characteristics Related to Structure. *Synth. Met.* **1997**, *88*, 171–177.

15. Conte, F.; Wang, S. H.; Péres, L. O.; Caseli, L. Colloids and Surfaces A : Physicochemical and Engineering Aspects Langmuir and Langmuir – Blodgett Films of a Quinoline-Fluorene Based Copolymer. *Colloids Surfaces A Physicochem. Eng. Asp.* **2012**, *394*, 67–73. https://doi.org/10.1016/j.colsurfa.2011.11.027.

16. Inukai, K.; Hotta, Y.; Tomura, S.; Takahashi, M.; Yamagishi, A. Preparation of the Langmuir - Blodgett Film of a Clay - Alkylammonium Adduct and Its Use as a Barrier for Interlayer Photoinduced Electron Transfer. *Langmuir* **2000**, *16*, 7679–7684. https://doi.org/10.1021/la9914312.

17. Petty, M. C. Possible Applications for Langmuir-Blodgett Films. *Thin Solid Films* **1992**, *210–211* (PART 2), 417–426. https://doi.org/10.1016/0040-6090(92)90300-Z.

18. Demond, A. H.; Lindner, A. S. Estimation of Interfacial Tension between Organic Liquids and Water. *Environ. Sci. Technol.* **1993**, *27* (12), 2318–2331. https://doi.org/10.1021/es00048a004.

19. Morita, T.; Singh, V.; Nagamatsu, S.; Oku, S.; Takashima, W.; Kaneto, K. Enhancement of Transport Characteristics in Poly(3-Hexylthiophene) Films Deposited with Floating Film Transfer Method. *Appl. Phys. Express* **2009**, *2*, 111502. https://doi.org/10.1143/APEX.2.111502.

20. Kawaguchi, M.; Tohyama, M.; Mutoh, Y.; Takahashi, A. Ellipsometric Study of Polymer Monolayers Spread at the Air-Water Interface. 1. Thickness of Monolayers. *Langmuir* **1988**, *4* (2), 407–410. https://doi.org/10.1021/la00080a025.

21. Kumaki, J. Polystyrene Monomolecular Particles Obtained by Spreading Dilute Solutions on the Water Surface. *Macromolecules* **1986**, *19* (8), 2258–2263. https://doi.org/10.1021/ma00162a025.

22. Noh, J.; Jeong, S.; Lee, J. Y. Ultrafast Formation of Air-Processable and High-Quality Polymer Films on an Aqueous Substrate. *Nat. Commun.* **2016**, *7*, 12374. https://doi.org/10.1038/ncomms12374.

23. Forester, R. H. Method of Producing an Ultrathin Polymer Film Laminate. US 3,551,244, 1970.

24. Mockus, L.; Reklaitis, G. V. Continuous Time Representation Approach to Batch and Continuous Process Scheduling . 1 . MINLP Formulation. *Ind. Eng. Chem. Res.* **1999**, *38*, 197–203. https://doi.org/10.1021/ie970311r.

25. Kumar, B.; Kaushik, B. K.; Negi, Y. S. Organic Thin Film Transistors: Structures, Models, Materials, Fabrication, and Applications: A Review. *Polym. Rev.* **2014**, *54* (1), 33–111. https://doi.org/10.1080/15583724.2013.848455.

26. Gevaerts, V. S.; Koster, L. J. A.; Wienk, M. M.; Janssen, A. J. Discriminating between Bilayer and Bulk Heterojunction Polymer : Fullerene Solar Cells Using the External Quantum Efficiency. *ACS Appl. Mater. Interfaces* **2011**, *3*, 3252–3255. https://doi.org/10.1021/am200755m.

27. Gilbert, L.; Weber, M. F.; Strharsky, R. J.; Stover, C. A.; Nevitt, T. J.; Ouderkirk, A. J. Giant Birefringent Optics in Multilayer Polymer Filters. *Science (80-.).* **2015**, *287*, 2451–2456. https://doi.org/10.1364/oic.2001.fa2.

28. Son, D.; Lee, J.; Qiao, S.; Ghaffari, R.; Kim, J.; Lee, J. E.; Song, C.; Kim, S. J.; Lee, D. J.; Jun, S. W.; et al. Multifunctional Wearable Devices for Diagnosis and Therapy of Movement Disorders. *Nat. Nanotechnol.* **2014**, *9* (5), 397–404. https://doi.org/10.1038/nnano.2014.38.

29. Moraes, M. R.; Alves, A. C.; Toptan, F.; Martins, M. S.; Vieira, E. M. F.; Paleo, A. J.; Souto, A. P.; Santos, W. L. F.; Esteves, F.; Zille, A. Glycerol / PEDOT : PSS Coated Woven Fabric as a Flexible Heating Element on Textiles †. *J. Mater. Chem. C* **2017**, *5*, 3807–3822. https://doi.org/10.1039/c7tc00486a.

30. Cohen, N.; David, Y.; Katz, N.; Milanovich, M.; Anavi, D.; Buzhor, M.; Amir, E. Electro-Conductive Fabrics Based on Dip Coating of Cotton in Poly (3-Hexylthiophene). *Polym. Adv. Technlogies* **2017**, *28* (August 2016), 583–589. https://doi.org/10.1002/pat.3857.

31. Bashir, T.; Skrifvars, M.; Persson, N. Production of Highly Conductive Textile Viscose Yarns by Chemical Vapor Deposition Technique : A Route to Continuous Process. *Polym. Adv. Technlogies* **2011**, *22*, 2214–2221. https://doi.org/10.1002/pat.1748.

32. Zhang, L.; Baima, M.; Andrew, T. L. Transforming Commercial Textiles and Threads into Sewable and Weavable Electric Heaters. *ACS Appl. Mater. Interfaces* **2017**, *9*, 32299–32307. https://doi.org/10.1021/acsami.7b10514.

33. Biglari, M. J.; Mokhtari, J.; Nouri, M.; Sarabi, A. A. Chemical Vapor Deposition of Poly (3-Alkylthiophene) Nanoparticles on Fabric : Chemical and Electrochemical Characterization. *J. Appl. Polym. Sci.* **2014**, 40673. https://doi.org/10.1002/app.40673.

34. Krebs, F. C. Fabrication and Processing of Polymer Solar Cells: A Review of Printing and Coating Techniques. *Sol. Energy Mater. Sol. Cells* **2009**, *93* (4), 394–412. https://doi.org/10.1016/j.solmat.2008.10.004.

35. O'Connor, B.; Pipe, K. P.; Shtein, M.; Connor, B. O.; Pipe, K. P.; Shtein, M. Fiber Based Organic Photovoltaic Devices. *Appl. Phys. Lett.* **2012**, *193306* (April 2008), 90–93. https://doi.org/10.1063/1.2927533.

36. Jinno, H.; Fukuda, K.; Xu, X.; Park, S.; Suzuki, Y.; Koizumi, M.; Yokota, T.; Osaka, I.; Takimiya, K.; Someya, T. Stretchable and Waterproof Elastomer-Coated Organic Photovoltaics for Washable Electronic Textile Applications. *Nat. Energy* **2017**, *2*, 780–785. https://doi.org/10.1038/s41560-017-0001-3.

37. Root, S. E.; Savagatrup, S.; Printz, A. D.; Rodriquez, D.; Lipomi, D. J. Mechanical Properties of Organic Semiconductors for Stretchable, Highly Flexible, and Mechanically Robust Electronics. *Chem. Rev.* **2017**, *117*, 6467–6499. https://doi.org/10.1021/acs.chemrev.7b00003.

38. Na, J. Y.; Kang, B.; Sin, D. H.; Cho, K.; Park, Y. D. Understanding Solidification of Polythiophene Thin Films during Spin-Coating: Effects of Spin-Coating Time and Processing Additives. *Sci. Rep.* **2015**, *5* (August), 1–14. https://doi.org/10.1038/srep13288.

39. Root, S. E.; Alkhadra, M. A.; Rodriquez, D.; Printz, A. D.; Lipomi, D. J. Measuring the Glass Transition Temperature of Conjugated Polymer Films with Ultraviolet-Visible Spectroscopy. *Chem. Mater.* **2017**, *29* (7), 2646–2654. https://doi.org/10.1021/acs.chemmater.7b00242.

40. Kleinschmidt, A. T.; Root, S. E.; Lipomi, D. J. Poly(3-Hexylthiophene) (P3HT): Fruit Fly or Outlier in Organic Solar Cell Research? *J. Mater. Chem. A* **2017**, *5* (23), 11396–11400. https://doi.org/10.1039/c6ta08317j.

41. Balar, N.; Rech, J. J.; Henry, R.; Ye, L.; Ade, H.; You, W.; O'Connor, B. T. The Importance of Entanglements in Optimizing the Mechanical and Electrical Performance of All-Polymer Solar Cells. *Chem. Mater.* **2019**, *31*, 5124–5132. https://doi.org/10.1021/acs.chemmater.9b01011.

42. Gao, L.; Zhang, Z. G.; Xue, L.; Min, J.; Zhang, J.; Wei, Z.; Li, Y. All-Polymer Solar Cells Based on Absorption-Complementary Polymer Donor and Acceptor with High Power Conversion Efficiency of 8.27%. *Adv. Mater.* **2016**, *28*, 1884–1890. https://doi.org/10.1002/adma.201504629.

43. Dang, M. T.; Hirsch, L.; Wantz, G. P3HT:PCBM, Best Seller in Polymer Photovoltaic Research. *Adv. Mater.* **2011**, *23* (31), 3597–3602. https://doi.org/10.1002/adma.201100792.

44. Root, S. E.; Jackson, N. E.; Savagatrup, S.; Arya, G.; Lipomi, D. J. Modelling the Morphology and Thermomechanical Behaviour of Low-Bandgap Conjugated Polymers and Bulk Heterojunction Films. *Energy Environ. Sci.* **2017**, *10* (2), 558–569. https://doi.org/10.1039/c6ee03456j.

45. Awartani, O.; Lemanski, B. I.; Ro, H. W.; Richter, L. J.; De Longchamp, D. M.; O'Connor, B. T. Correlating Stiffness, Ductility, and Morphology of Polymer:Fullerene Films for Solar Cell Applications. *Adv. Energy Mater.* **2013**, *3* (3), 399–406. https://doi.org/10.1002/aenm.201200595.

46. Keum, H.; Mccormick, M.; Liu, P.; Zhang, Y.; Omenetto, F. G. RESEARCH ARTICLES Epidermal Electronics. *Science (80-.).* **2011**, *333* (September), 838–844.

47. Savagatrup, S.; Printz, A. D.; Rodriquez, D.; Lipomi, D. J. Best of Both Worlds: Conjugated Polymers Exhibiting Good Photovoltaic Behavior and High Tensile Elasticity. *Macromolecules* **2014**, *47*, 1981–1992. https://doi.org/10.1021/ma500286d.

48. Spano, F. C. The Spectral Signatures of Frenkel Polarons in H- and J-Aggregates. *Acc. Chem. Res.* **2010**, *43* (3), 429–439.

49. Böckmann, M.; Schemme, T.; De Jong, D. H.; Denz, C.; Heuer, A.; Doltsinis, N. L. Structure of P3HT Crystals, Thin Films, and Solutions by UV/Vis Spectral Analysis. *Phys. Chem. Chem. Phys.* **2015**, *17* (43), 28616–28625. https://doi.org/10.1039/c5cp03665h.

50. Sparavigna, A. C.; Florio, L.; Avloni, J.; Henn, A. Polypyrrole Coated PET Fabrics for Thermal Applications. *Mater. Sci. Appl.* **2010**, *2010* (October), 253–259. https://doi.org/10.4236/msa.2010.14037.

51. Wang, Y.; Zhan, X. Layer-by-Layer Processed Organic Solar Cells. *Adv. Energy Mater.* **2016**, *6*, 1–18. https://doi.org/10.1002/aenm.201600414.

52. Hintz, H.; Egelhaaf, H. J.; Lüer, L.; Hauch, J.; Peisert, H.; Chassé, T. Photodegradation of P3HT - A Systematic Study of Environmental Factors. *Chem. Mater.* **2011**, *23* (2), 145–154. https://doi.org/10.1021/cm102373k.

Chapter 3. Stability of Perovskite Films Encapsulated in Single- and Multi-Layer Graphene Barriers

3.1 Introduction

The stability of perovskite solar cells (PSCs) remains as one of the major challenges on the path of their commercialization and deployment.[1] While the record efficiencies of PSCs continue to rise,[2,3] their sensitivity to environmental factors such as moisture,[4,5] oxygen,[6] temperature,[7] and light[8,9] limit their economic and practical viability. To address these concerns, researchers have undertaken several lines of inquiry in order to extend the lifetimes of PSCs. These areas of research focus fall broadly into three categories: (1) the development of new perovskite compositions with greater intrinsic stability (e.g. mixed cation and/or halides);[10–13] (2) the optimization of interfaces within devices, so as to minimize defects and vacancies;[4, 6,14,15] and (3) the encapsulation of devices in order to slow the ingress of moisture and oxygen.[16–20] Our work here focuses predominantly on the third of these research thrusts.

To measure the stability against these stressors, researchers often use accelerated degradation studies, in which materials or whole devices are subjected to extreme conditions that simulate long-term degradation. Recently, the research community has attempted to standardize testing protocols to aid in the comparison of stability measured in different laboratories.[21] For example, the vulnerability of perovskites to heat, moisture, and oxygen can be simultaneously evaluated using “damp heat testing,” in which devices or films are subjected to high temperatures and humidity in order to rapidly simulate the effects of long-term degradation.[4–6,22,23] These accelerated testing conditions have proven to be a challenging stability threshold for perovskite photovoltaics to overcome due to their intrinsic sensitivity to oxygen and water.[5, 16,24–26] One obstacle in devising scalable encapsulation schemes for PSC is that typical materials used for encapsulation of solar cells or other semiconductors—typically ethylene vinyl acetate or other polyolefins—require processing temperatures often ~ 150 °C.[27,28] In PSCs, however, such

temperatures can destabilize the perovskite absorber, the hole-transport layer (HTL), or both.[29,30] As a result, PSCs often exhibit a reduction in efficiency after encapsulation,[23] and relatively long-lasting PSCs have a lower efficiency compared to record devices.[31] It is therefore critical to investigate new barrier materials and encapsulation techniques that are compatible with PSCs.

Graphene is an intriguing material for thin-film, flexible barriers due to the impermeability of its basal plane to gases[32] as well as its high optical transmissivity.[33] In this paper we investigate the efficacy of graphene barriers towards preventing the degradation of perovskite films, using an encapsulation scheme shown in Figure 3.1. The use of a low-temperature-activating poly(iso-butylene) (PIB) edge seal results in a high-quality encapsulation without causing degradation of the film, and ensures that any small species ingress is through the barrier film being investigated.[16,34,35] Numerous papers already speculate an enhancement to the stability of perovskite solar cells (PSCs) when encapsulated with graphene.[4,36] Graphene derivatives, including fluorine-doped nano platelets[37] and graphene oxides,[38,39] have also been shown to increase the stability of PSCs. Various studies have also incorporated graphene into PSCs as an electrode material (due to the electrical conductivity of graphene) either in combination with or separate from barrier applications.[40,41] Nonetheless, the presence of grain boundaries and defects within CVD graphene can provide numerous permeation pathways for species such as water and oxygen.[42] As a result, many reports of improved PSC stability due to encapsulation with graphene may not be due entirely to graphene itself, but rather aided by the polymeric support layer on which the graphene is adhered.

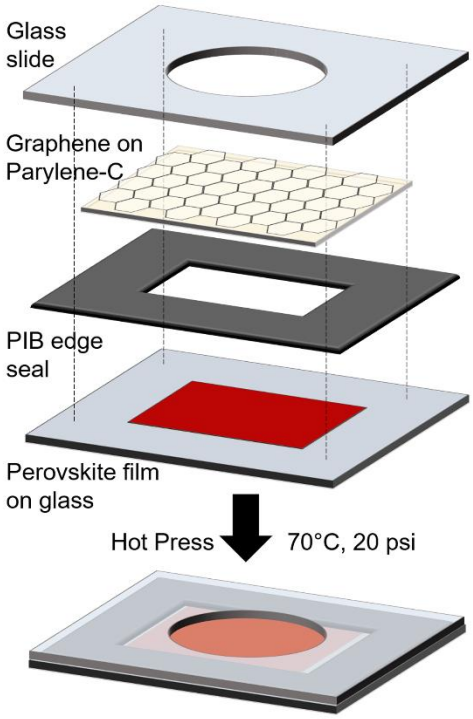

Figure 3.1 Schematic drawing of the encapsulation process.

One method to reduce availabilities of these pathways for the permeation of gases is by stacking multiple monolayers of graphene. With multiple layers, transport through grain boundaries and pinholes may become blocked by adjoining layers.[43] Here we measure the performance of barriers composed of up to three layers of graphene (Figure 3.2a), beyond which the cost, complexity of fabrication, and optical losses (2.3% per layer of graphene)[33] (Figure 3.2b) would be impractical for optoelectronic devices, such as thin-film solar cells.

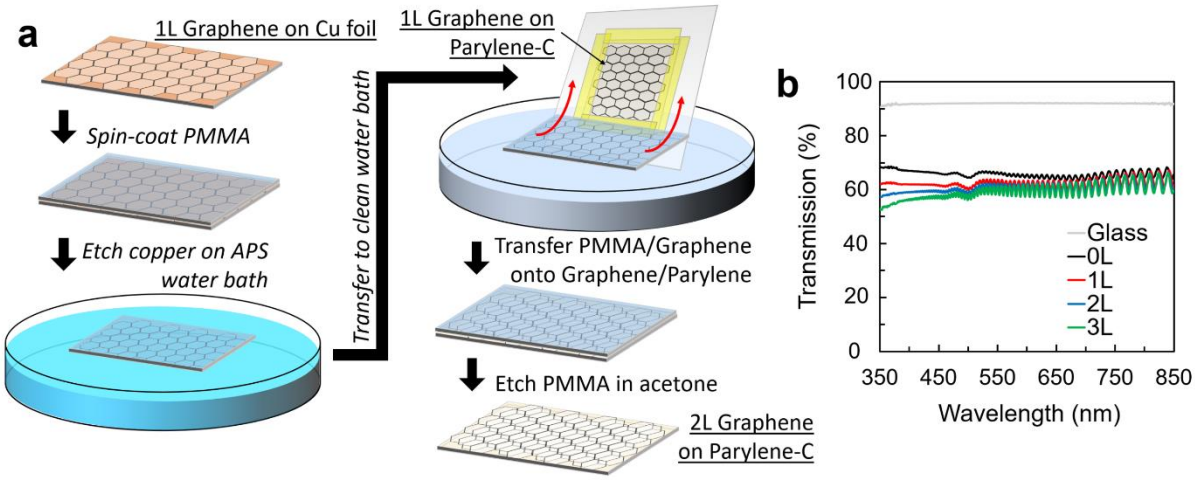

Figure 3.2 Preparation of multi-layer graphene barrier films. (a) Schematic illustration of fabrication of 2-layer graphene on parylene. (b) UV-vis transmission spectra of graphene-on-parylene barriers as a function of the number of graphene layers.

3.2 Materials and Methods

3.2.1 Materials

Formamidinium iodide (FAI) and methylammonium bromide (MABr) were purchased from GreatCell Solar Materials. CsI (99.999% purity), DMSO (99.9% purity), DMF (99.9% purity), and chlorobenzene (99.9% purity) were purchased from Sigma-Aldrich. PbI_2 (99.99% purity) and $PbBr_2$ (99.99% purity) were purchased from TCI. Poly(methyl methacrylate) (PMMA, M_w = 550,000) was obtained from Alfa Aesar. Ammonium persulfate (APS) and anisole were obtained from Acros Organics. Prior to use, all solvents were dried for 24 h with 3Å molecular sieves (VWR, grade 564, mesh 8-12) then filtered with a 0.22 µm PTFE syringe filter. Monolayer CVD graphene on copper foil and monolayer graphene mounted on 10 µm parylene-C were supplied by Grolltex, Inc, with a >95% surface coverage of graphene as determined by optical microscopy. Polyisobutylene (PIB) edge seal sheets were obtained from Quanex.

3.2.2 Preparation of Graphene Barriers

Monolayer graphene on 10 µm parylene-C (hereafter referred to as 1L) was used as is. The procedure we used to prepare 2-layer (2L) and 3-layer (3L) graphene on parylene-C involves iterative deposition of monolayer graphene,[44,45] shown in Figure 3.2a. Briefly, monolayer graphene on copper foil (5 cm × 5 cm) was spin-coated with a 4 wt% PMMA solution in anisole at 4000 rpm for 60 s. After annealing at 150 °C for 5 min to remove any remaining anisole, the copper was etched in a 0.05 g/mL solution of APS in water for 2 h, until fully dissolved. The resulting floating PMMA/graphene was transferred to a clean water bath. Separately, a 5 cm × 5 cm piece of 1L graphene was taped to a glass slide, graphene facing up. The PMMA/graphene was transferred directly onto the 1L film, with the two graphene layers in direct contact, and allowed to dry overnight in a desiccator. Finally, the PMMA was removed by etching in a 50 °C bath of acetone for 5 min, then rinsed with IPA and allowed to dry. This process was repeated once more to yield 3-layer graphene. Successful graphene transfer was confirmed via UV-vis (Figure 3.2b) showing a successive decrease in optical transmission with each layer of graphene added. Lastly, 0L graphene (aka plain 10 µm parylene-C) was obtained by treating 1L films with plasma (30 W) for 30 s at a base pressure of 250 mTorr of air. Graphene removal was confirmed via sheet resistance measurements which showed no conductivity in the resulting films, as well as UV-vis showing an increase in optical transmission (Figure 3.2b).

3.2.3 Preparation of Perovskite Films

Substrates—glass or fluorine-doped tin oxide (FTO)—were cleaned through a series of sonication (15 min) and rinse steps in the following sequence: 2 v% Hellmanex in DI water, DI water, isopropanol, and acetone. Afterward, the substrates were rinsed in IPA and dried with compressed air.

The triple cation perovskite films were prepared in a nitrogen-filled glovebox. First, two separate solutions of 1.5 M lead iodide and 1.5 M lead bromide were prepared with a 9:1 volume ratio of DMF and DMSO used as a solvent. The solutions were vortexed then heated to 100 °C for 10 min. The PbI_2 solution was added to FAI and $PbBr_2$ solution was added to MABr such that 1.22 M solutions of $FAPbI_3$ and $MAPbBr_3$, respectively, with a 1.09 over-stoichiometric ratio of the lead salts were formed (using the 9:1 DMF:DMSO solution to dilute as necessary). An additional solution of 1.5 M CsI in DMSO was prepared in the glovebox and heated at 150 °C for 10 min. The $FAPbI_3$ and $MAPbBr_3$ solutions were mixed together in a 5:1 ratio and 5% molar ratio (with respect to the A-site) of CsI was added to the final solution resulting in a nominal stoichiometry of $FA_{0.79}MA_{0.16}Cs_{0.05}Pb(I_{0.84}Br_{0.16})_3$.

The perovskite films were formed by spin coating. Prior to deposition the substrates were treated with air-based plasma for 10 min at 300 mTorr. 90 µL of solution was dropped onto the substrate and doctor bladed across the entire surface. The first step of the spin-cast at 1000 RPM for 10 s served to remove excess solution and ensure an even spread across the entirety of the substrate. In the second step, the speed was increased to 5500 RPM for 20 s. 250 µL of chlorobenzene was dispensed rapidly (in approximately 1 s) after 8 s had expired in step 2 of the spin-coat. The films were annealed on a hotplate for 45 min at 100°C, resulting in a final thickness of 550 nm.

3.2.4 Encapsulation of Films

The assembly of the encapsulated films is shown in Figure 3.1. After spin-coating of the perovskite films, the edges of the film (approximately 0.5 cm) were wiped away with methoxyethanol and a cotton swab. PIB edge seal sheets were cut into 2.5 cm × 2 cm rectangles, from which a 2 × 1.5 cm rectangle was cut out from the center. Barrier films were cut to 2.25 × 1.75 cm rectangles and placed onto glass slides which had a 1-cm hole drilled out from the center. Adhesive PIB edge seal pieces were then placed on top, and pressed with tweezers to hold in

place. These barrier/glass slides were then transferred to the glovebox, where perovskite films were pressed onto the PIB edge seal. The films were then placed onto a hot plate at 70°C, under a mass exerting a pressure of 20 psi to activate the edge seal. After 20 min, samples were removed from the hot plate, and allowed to cool. For samples encapsulated in glass, a 2.5 × 2 cm glass slide was adhered with PIB edge seal directly onto the perovskite film. Additional control (exposed) samples with no barrier were also prepared.

3.2.5 Film Monitoring

Samples were placed into a humidity chamber at 65 °C, 85% relative humidity (ISOS-D-3 testing protocol).[21] Films were removed from the humidity chamber at regular intervals and analyzed via photoluminescence measurements and UV-Vis spectroscopy. Photoluminescence measurements were taken using a Renishaw Raman/microPL microscope with a 633 nm excitation laser, 600 mm^{-1} grating. UV-vis measurements were taken on a Perkin Elmer LAMBDA 1050+ UV/Vis/NIR Spectrophotometer. For each condition, five films were prepared and aged while two films were actively monitored. At the end of the aging test, the encapsulation was removed from films to enable analysis via x-ray diffraction (XRD). XRD measurements were taken using a Rigaku SmartLab diffractometer. Pictures of the films before and after aging for 200 h are shown in Figure 3.3.

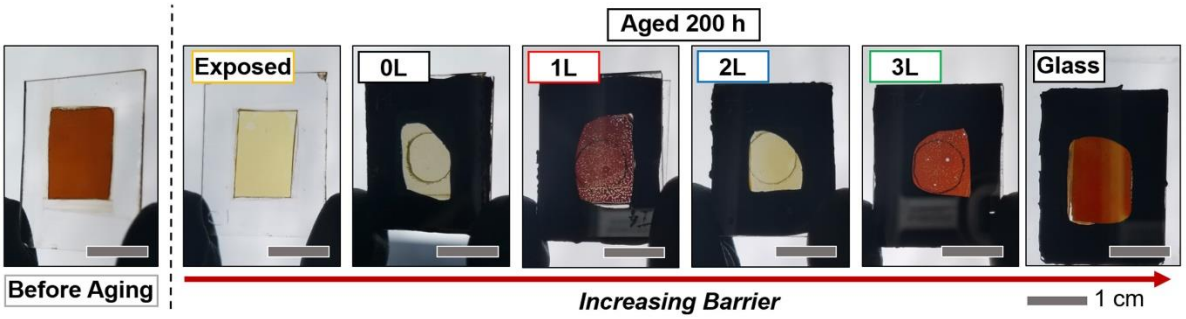

Figure 3.3 Pictures of representative films before and after aging for 200 h.

3.3 Results and Discussion

The optical absorbance evolution of select perovskite films is shown in Figure 3.4a-c. As seen in Figure 3.4a, the exposed films quickly tended towards optical transparency, retaining only a small amount of absorbance at shorter (purple) wavelengths (and thus appearing light yellow—see Figure 3.3). This trend is attributed to the degradation to and subsequent outgassing of volatile species (such as methylammonium iodide and HI) from the perovskite film.[46] Figure 3.4b shows the UV-vis evolution for the 1L-encapsulated films, where the decrease in absorbance was also observed but was less rapid. The 0L, 2L and 3L graphene/parylene samples showed similar behavior. Finally, the glass-encapsulated films (Figure 3.4c) showed minimal variation in absorbance during aging, confirming the quality of the PIB edge seal as well as the strong thermal stability of the perovskite (the glass-encapsulated samples were left to age an additional 800 h after the remaining samples were removed from the humidity chamber, and still displayed minimal signs of degradation). We observed distinct absorbance profiles between the exposed/0L/2L samples and the 1L/3L samples. The former set showed a marked decrease in absorbance at longer wavelengths, which we attribute to the conversion of perovskite into PbI_2, which is optically absorbent only below 550 nm.[47] The latter set, in contrast, continued to absorb light up to 750 nm throughout the aging test, due to the continued presence of perovskite. These observations are clarified by considering absorbance at 450 nm (where absorbance from the triple cation perovskite, δ-$FAPbI_3$,[48] and PbI_2 are observed) and at 700 nm (which is only absorbed by the perovskite. In Figure 3.4d, the ratio of absorbance between 450 nm and 700 nm are shown as a function of time. Here, the 1L/3L samples retained ~2× more absorbance at longer wavelengths than the 0L/2L samples, which themselves were ~3×more absorbent than the exposed film. Additionally, when the time evolution of absorbance at 700 nm is considered (Figure 3.4e), we observe that 3L retains much more perovskite relative to the other barrier films. However, significant loss is still realized even in the 3L condition. Figure 3.3, showing photos of the aged

film, also mirrors this trend, with the exposed/0L/2L films appearing yellow, compared to the red-colored 1L/3L films (though visually, some spottiness is apparent in the 1L/3L films, indicative of degradation in those films as well). The 2L graphene exhibits worse performance than the 1L due to the handling required to coat the additional graphene layer onto the commercial 1L graphene/parylene (see Figure 3.2), which can induce defects/tears in graphene.[49] The decrease of performance upon the addition of a second graphene layer was observed across all five films that were aged. Additionally, multiple sets of 2L films prepared from different batches of graphene exhibited diminished performance as confirmed by conductivity and Raman measurements.

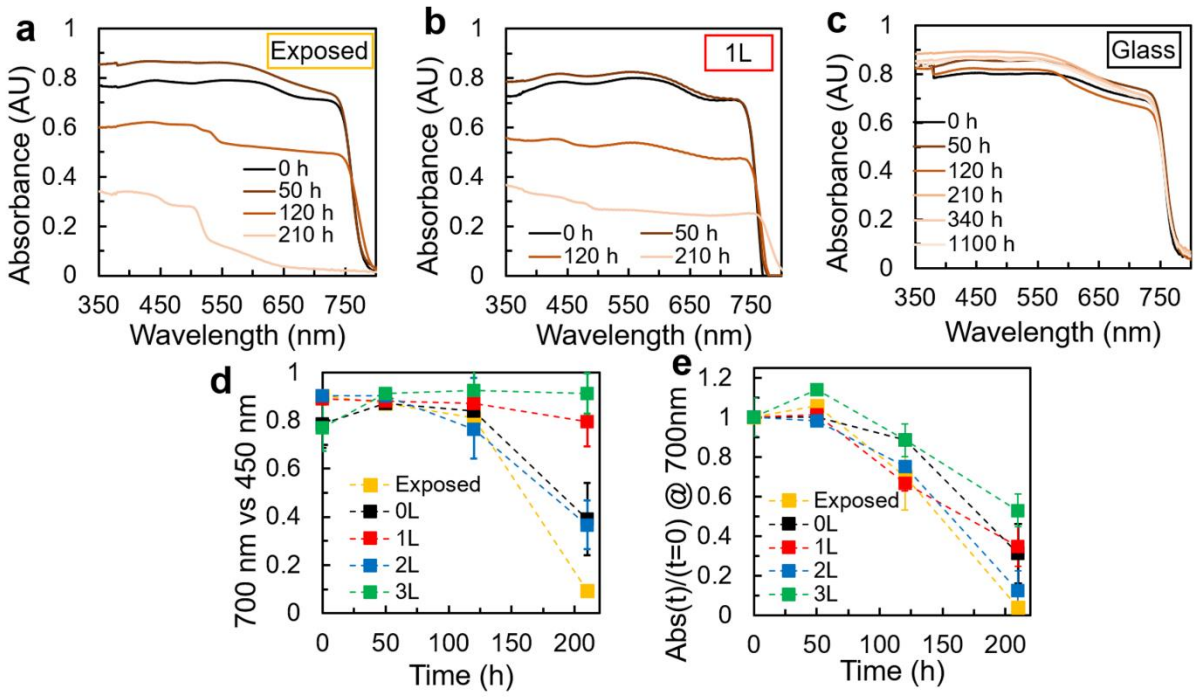

Figure 3.4 UV-Vis tracking during perovskite film aging. (a-c) Evolution of UV-vis spectra for (a) exposed, (b) 1L, and (c) glass-encapsulated films. Remaining UV-vis spectra are given in Figure S1. (d) Ratio of absorbance intensity at 700 nm vs 450 nm. (e) Ratio of absorbance intensity at 700 nm at t vs t=0.

To complement the information gained from tracking optical absorbance, we also monitored the films' photoluminescence (PL) behavior over time, which can give insight into the films' optoelectronic properties. These results are shown in Figure 3.5. To improve readability, the evolution of the peak PL intensity (Figure 3.5a-b) and peak PL wavelength (Figure 3.5c-d) have

each been split into 2 panels, with the same data from the 1L-encapsulated sample represented in both panels. As shown in Figure 3.5a, all of the graphene/parylene films exhibit an increase in PL over time, despite becoming yellow/spotty during aging (Figure 3.3). In early trials, we considered that this phenomenon could be due to condensation forming on the graphene/parylene barrier, potentially amplifying the PL emissions back to the detector. Thus, in later trials we carefully dried the exposed barrier films with an air gun prior to every PL measurement, and this phenomenon persisted. In contrast, the exposed films exhibited no photoluminescence under laser excitation by 100 h, while the glass-encapsulated films showed only a slight increase in PL emission. (Figure 3.5b). In addition, the graphene/parylene-encapsulated samples exhibited a shift in the peak wavelength of PL emissions (Figure 3.5c), a behavior not present in the glass films, and only minimally observed in exposed films (Figure 3.5d).

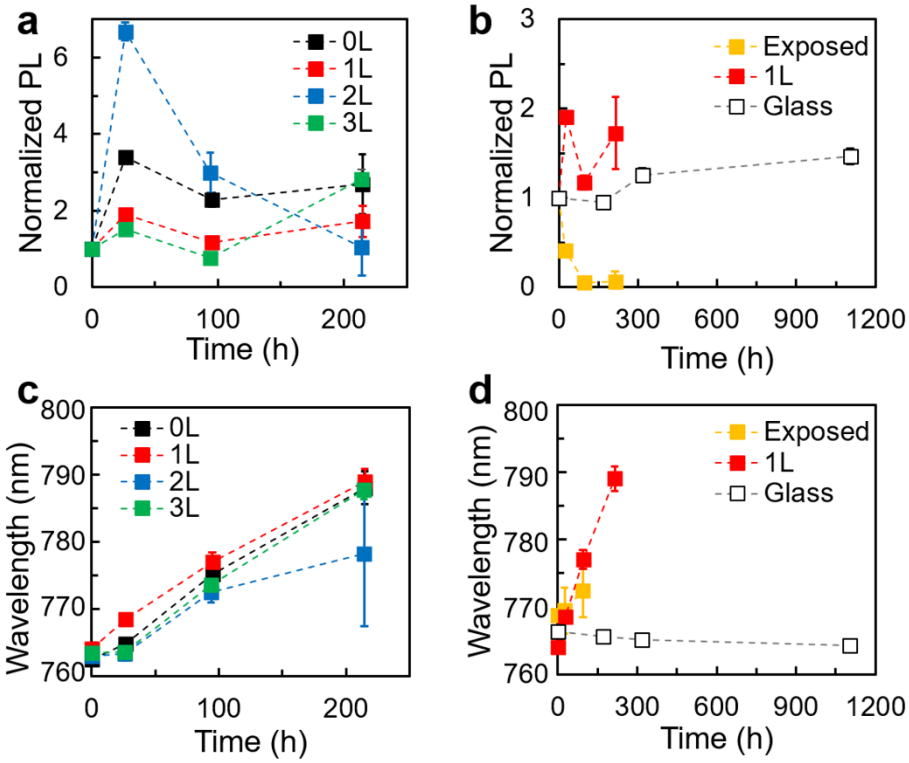

Figure 3.5 Photoluminescence (PL) evolution during aging. (a) Normalized average PL evolution for 0, 1, 2 and 3L-graphene. (b) PL evolution comparing 1L to glass and control samples. (c) Peak PL wavelength evolution for 0, 1, 2 and 3L-graphene. (d) Evolution of peak PL wavelength comparing 1L to glass and exposed samples.

Further understanding the differences in perovskite decay was achieved via probing the crystallographic properties of the films through x-ray diffraction (XRD). The x-ray diffractograms for our films before and after aging for 200 h are shown in Figure 3.6a. The glass-encapsulated films remained virtually unchanged compared to films analyzed before aging, in alignment with the trends observed with UV-Vis and PL. In contrast, the graphene/parylene films all exhibited a substantial decrease in intensity of the triple cation perovskite peak at 2θ = 14°, while also gaining a prominent peak at 2θ = 11.5°, corresponding to the hexagonal δ-$FAPbI_3$. The δ-$FAPbI_3$ peak is not seen in either the exposed or glass-encapsulated films; it formed only in the presence of the semi-permeable parylene encapsulation material.

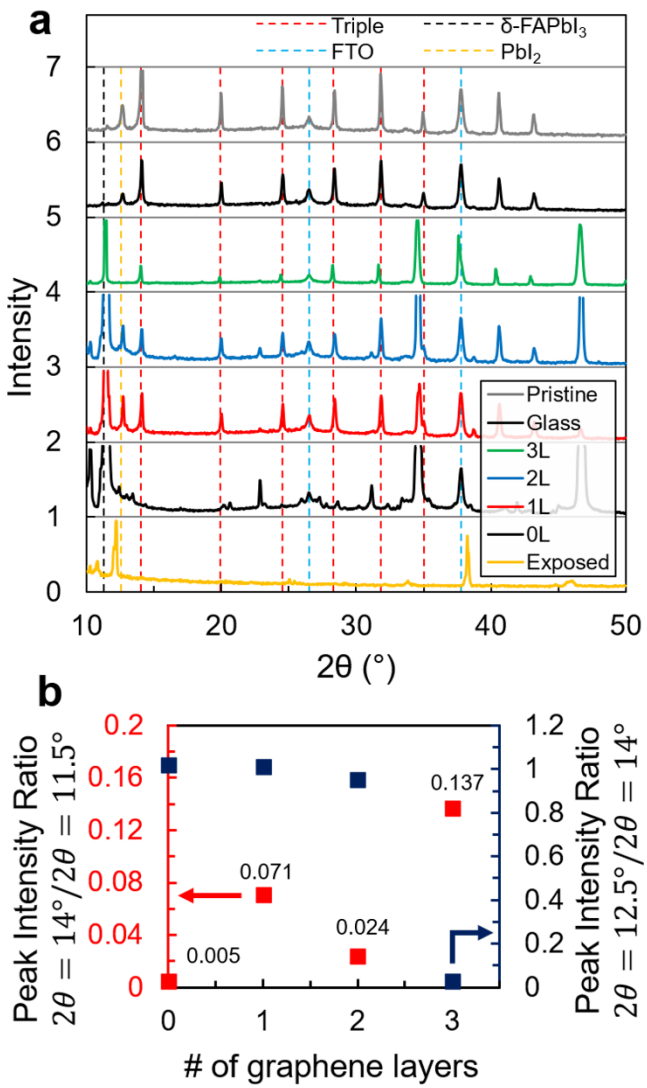

Figure 3.6 XRD analysis of perovskite films. (a) XRD diffractograms for films before and after aging. (b) Ratio of peak intensity of triple cation perovskite (2θ = 14°) to peak intensity of δ-$FAPbI_3$ (2θ = 11.5°) and PbI_2 peak intensity (2θ = 12.5°) as a function of number of layers of graphene.

The x-ray diffractograms also allow for qualitative estimation of the relative degree of conversion between triple cation perovskite and δ-$FAPbI_3$ between the graphene/parylene films, by comparing the intensities of the peaks at 14° and 11.5°.[7] This ratio is plotted in Figure 3.6b, and shows the dramatic effect that the addition of graphene conveys to the parylene support layer. While the triple cation perovskite in the 0L graphene has almost completely decayed into δ-$FAPbI_3$, the 1L graphene film has a 15× higher ratio of triple cation to δ-$FAPbI_3$, which itself is nearly doubled again between the 1L and 3L graphene. Meanwhile, the 2L films exhibited worse

performance than either the 1L or 3L films, a similar trend as seen via optical absorbance and PL emission. The addition of a 3rd layer of graphene (3L) appears able to negate and improve upon any damaging wrinkles/tears induced by the multi-layer graphene preparation.

These observations suggest that our set of films have undergone three unique degradation pathways. The first, seen in the exposed films, is the degradation of the triple cation perovskite into PbI_2,[50] along with the expulsion of all volatile species. The second, observed in the glass-encapsulated samples, is a slow thermal anneal due to the elevated temperature (85°C) of the humidity chamber used for the accelerated decay test. The effect is a reduction of non-radiative recombination centers (leading to a slight PL increase) without changes to the chemical composition of the films, as there is no pathway for species ingress/egress. The final degradation pathway observed, seen in the graphene/parylene films, is the phase segregation and formation of multiple perovskite phases, particularly iodide-rich and bromide-rich domains. This is exhibited by the increased and red-shifted PL profile, which is attributed to the iodine-rich phases acting as a carrier sink.[51] Additionally, photoinactive phases (such as δ-$FAPbI_3$ and potentially I_2[50]) are forming, due to the ingress of oxygen and water.[52]

More detailed analysis of the graphene barriers, separate from the perovskite films, was carried out in order to validate our findings. Figure 3.7a shows the sheet resistance of the graphene films. The increasing conductivity as each layer is added, as well as overall magnitude of sheet resistance, are consistent with previous reports.[44] The average optical transmissivity of the films (Figure 3.7b) likewise shows a successive change with each layer added, further confirming successful transfer. In contrast, air permeability measurements (Figure 3.7c) show a large (15×) decrease between 0L and 1L, followed by smaller variations from 1L to 2L to 3L. Notably, the difference between the permeability of 0L vs 1L films is identical the difference in ratio of the triple cation perovskite/δ-$FaPbI_3$ shown in Figure 3.6b. Meanwhile, the minimal variations in air permeability between the single- and multi-layer graphene barriers are in sharp

contrast to the varied perovskite degradation observed, with 2L films decaying substantially compared to 1L and 3L films.

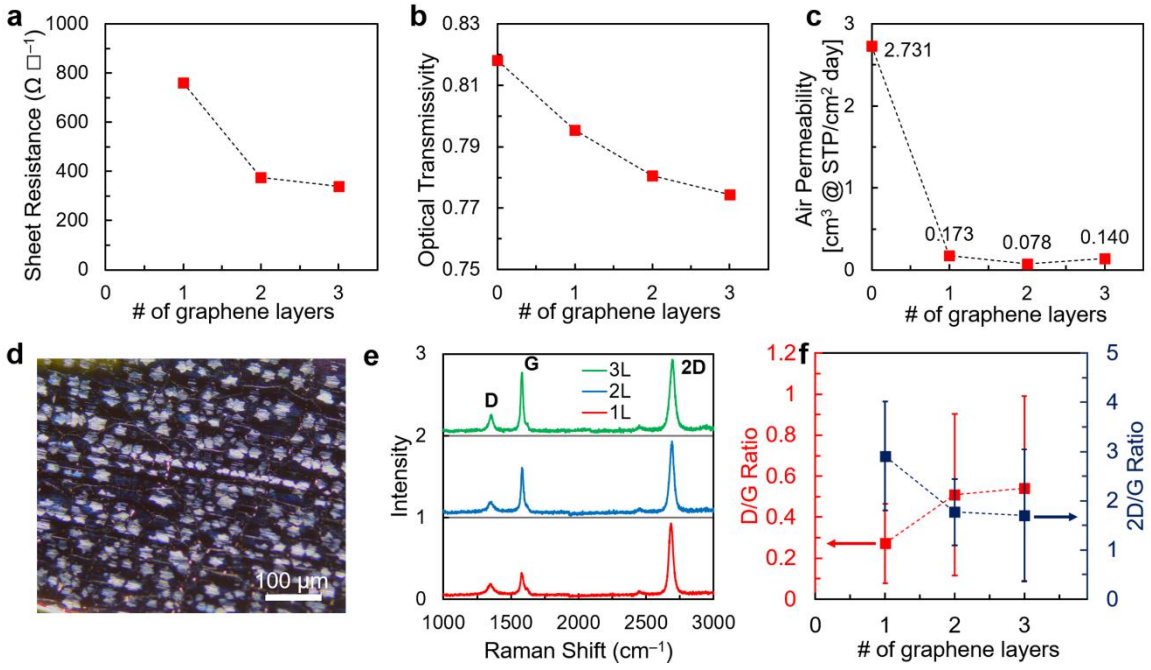

Figure 3.7 Analysis of single- and multi-layer graphene barrier films. (a) Sheet resistance of films as a function of number of layers (0L films produced an open circuit). (b) Average optical transmissivity (extracted from Figure 3.2b). (c) Air permeability of films, found using an isochoric gas permeability apparatus. (d) Optical micrograph of 1L graphene, as received. (e) Representative Raman spectra of 1L, 2L and 3L graphene films. (f) Average D/G and 2D/G ratio for graphene films.

To investigate this discrepancy, spatial mapping using Raman was conducted in order to analyze the quality of the graphene films and spatial resolution. We note that Raman analysis cannot be done directly onto the parylene films, whose spectra overwhelm the graphene signal, and must instead be measured following water transfer onto a silicon substrate. The overlain spectra for 30 measurements for 1L graphene show a wide range of graphene quality, and numerous traces show minimal or no graphene signal. Indeed, the spatial coverage of transferred graphene was less than 50% for both 1L and 2L films, coupled with large variability in the 2D/G ratio (Figure 3.6), which gives information regarding the number of monolayers of graphene.[53] Several factors likely influence the lack of uniformity and variability in coverage of the graphene films. First, nanoislands and macroscopic regions of multilayer graphene are commonly found on

CVD-grown graphene (see Figure 3.7d), and are formed via nucleation from silica or other impurities within the copper foil on which it is grown;[54,55] thus, a uniform monolayer of graphene is unlikely to be present in the 1L films to begin with. Additionally, the water transfer method for layer-by-layer growth of multilayer graphene is easily susceptible to wrinkling and tearing.[49] Although previous work by Yoon, et al. on multilayer graphene films (prepared via the same method as our own films) claims that that strong van der Waals forces between graphene layers can fully suppress lateral diffusion of air molecules,[56] the authors note that in cracked regions, air molecules will indeed diffuse laterally, allowing them to access adjoining grain boundaries and pinholes and permeate vertically through the film. We note that a graphene grain boundary typically refers to a tilt grain boundary comprised of 5- and 7- membered rings,[57,58] through which small species are able to permeate.[59] The wide variability in graphene uniformity and coverage in our multilayer (i.e. 2L and 3L) films will therefore result in highly variable barrier properties over a large (~cm^2) area. Given the penalties of increased process complexity and materials cost of each successive layer of graphene used, compared to the small improvement in perovskite film stability shown between 1L and 3L graphene, we conclude that 1L graphene may offer the best combination of properties for use in flexible, optically transparent barrier applications for perovskite films. Beyond single- and multi-layer graphene, other 2D materials may prove to be intriguing for similar encapsulation applications. As an example, graphene oxide also exhibits good barrier performance against air and water,[60] although thickness would need to be carefully controlled to retain optical transmissibility.[61] Meanwhile, hexagonal boron nitride has recently emerged as a promising new 2D material and exhibits excellent transparency due to its wide bandgap,[62] although it tends to have smaller grains than CVD graphene,[63] which could exacerbate the leakage issues we observed.

3.4 Conclusion

Experimental results show that single-layer graphene can confer substantially improved barrier performance to a polymeric support film, with multi-layer (at least 3L) graphene yielding further improved barrier performance. We emphasize that 2L graphene exhibited worse performance as an encapsulant than 1L graphene, most likely due to defects introduced during manipulation of the films. Nevertheless, all of our graphene/parylene-encapsulated films showed substantial degradation compared to glass-encapsulated films, suggesting that for rigid, non-flexible, long-lasting applications, the addition of graphene to a semi-permeable flexible polymer barrier is insufficient for generating a highly stable device. While modifications to the preparation procedure of the multi-layer graphene could result in improved barrier performance, the numerous grain boundaries in CVD graphene still result in a bulk material that is far from attaining the "impermeable" status of glass or molecular graphene. Still, the substantial improvement obtained from the addition of a single layer of graphene to our polymer support layer makes graphene-based barriers a compelling potential encapsulant for lightweight and/or flexible perovskite solar cells.

Chapter 3, in full, is a reprint of the material "Stability of Perovskite Films Encapsulated in Single- and Multi-Layer Graphene Barriers" as it appears in ACS Applied Energy Materials, by Runser, R., Kodur, M., Skaggs, J.D., Cakan, D.N., Foley, J.B., Finn, M., Fenning, D.P., and Lipomi, D.J., 2021, 10314–10322. The dissertation author was the first author of this paper, all authors contributed to this work.

3.5 References

1. K. Rao, M.; Sangeetha, D. N.; Selvakumar, M.; Sudhakar, Y. N.; Mahesha, M. G. Review on Persistent Challenges of Perovskite Solar Cells' Stability. *Sol. Energy* **2021**, *218* (February), 469–491. https://doi.org/10.1016/j.solener.2021.03.005.

2. Jeong, J.; Kim, M.; Seo, J.; Lu, H.; Ahlawat, P.; Mishra, A.; Yang, Y.; Hope, M. A.; Eickemeyer, F. T.; Kim, M.; Yoon, Y. J.; Choi, I. W.; Darwich, B. P.; Choi, S. J.; Jo, Y.; Lee, J. H.; Walker, B.; Zakeeruddin, S. M.; Emsley, L.; Rothlisberger, U.; Hagfeldt, A.; Kim, D. S.; Grätzel, M.; Kim, J. Y. Pseudo-Halide Anion Engineering for α-FAPbI3 Perovskite Solar Cells. *Nature* **2021**, *592* (September 2020). https://doi.org/10.1038/s41586-021-03406-5.

3. Green, M. A.; Dunlop, E. D.; Hohl-Ebinger, J.; Yoshita, M.; Kopidakis, N.; Ho-Baillie, A. W. Y. Solar Cell Efficiency Tables (Version 55). *Prog. Photovoltaics Res. Appl.* **2020**, *28* (1), 3–15. https://doi.org/10.1002/pip.3228.

4. Hu, X.; Jiang, H.; Li, J.; Ma, J.; Yang, D.; Liu, Z.; Gao, F.; Liu, S. Air and Thermally Stable Perovskite Solar Cells with CVD-Graphene as the Blocking Layer. *Nanoscale* **2017**, *9* (24), 8274–8280. https://doi.org/10.1039/c7nr01186e.

5. Song, Z.; Abate, A.; Watthage, S. C.; Liyanage, G. K.; Phillips, A. B.; Steiner, U.; Graetzel, M.; Heben, M. J. Perovskite Solar Cell Stability in Humid Air: Partially Reversible Phase Transitions in the PbI2-CH3NH3I-H2O System. *Adv. Energy Mater.* **2016**, *6* (19). https://doi.org/10.1002/aenm.201600846.

6. Habisreutinger, S. N.; Leijtens, T.; Eperon, G. E.; Stranks, S. D.; Nicholas, R. J.; Snaith, H. J. Carbon Nanotube/Polymer Composites as a Highly Stable Hole Collection Layer in Perovskite Solar Cells. *Nano Lett.* **2014**, *14* (10), 5561–5568. https://doi.org/10.1021/nl501982b.

7. Akbulatov, A. F.; Luchkin, S. Y.; Frolova, L. A.; Dremova, N. N.; Gerasimov, K. L.; Zhidkov, I. S.; Anokhin, D. V.; Kurmaev, E. Z.; Stevenson, K. J.; Troshin, P. A. Probing the Intrinsic Thermal and Photochemical Stability of Hybrid and Inorganic Lead Halide Perovskites. *J. Phys. Chem. Lett.* **2017**, *8* (6), 1211–1218. https://doi.org/10.1021/acs.jpclett.6b03026.

8. Tan, W.; Bowring, A. R.; Meng, A. C.; McGehee, M. D.; McIntyre, P. C. Thermal Stability of Mixed Cation Metal Halide Perovskites in Air. *ACS Appl. Mater. Interfaces* **2018**, *10* (6), 5485–5491. https://doi.org/10.1021/acsami.7b15263.

9. Kanda, H.; Usiobo, O. J.; Momblona, C.; Abuhelaiqa, M.; Sutanto, A. A.; Igci, C.; Gao, X. X.; Audinot, J. N.; Wirtz, T.; Nazeeruddin, M. K. Light Stability Enhancement of Perovskite Solar Cells Using 1H,1H,2H,2H-Perfluorooctyltriethoxysilane Passivation. *Sol. RRL* **2021**, *5* (3), 1–7. https://doi.org/10.1002/solr.202000650.

10. Ono, L. K.; Juarez-Perez, E. J.; Qi, Y. Progress on Perovskite Materials and Solar Cells with Mixed Cations and Halide Anions. *ACS Appl. Mater. Interfaces* **2017**, *9* (36), 30197–30246. https://doi.org/10.1021/acsami.7b06001.

11. Cai, Y.; Wang, S.; Sun, M.; Li, X.; Xiao, Y. Mixed Cations and Mixed Halide Perovskite Solar Cell with Lead Thiocyanate Additive for High Efficiency and Long-Term Moisture Stability. *Org. Electron.* **2018**, *53* (November 2017), 249–255. https://doi.org/10.1016/j.orgel.2017.11.045.

12. Saliba, M.; Matsui, T.; Domanski, K.; Seo, J. Y.; Ummadisingu, A.; Zakeeruddin, S. M.; Correa-Baena, J. P.; Tress, W. R.; Abate, A.; Hagfeldt, A.; Grätzel, M. Incorporation of Rubidium Cations into Perovskite Solar Cells Improves Photovoltaic Performance. *Science (80-.).* **2016**, *354* (6309), 206–209. https://doi.org/10.1126/science.aah5557.

13. Saliba, M.; Matsui, T.; Seo, J. Y.; Domanski, K.; Correa-Baena, J. P.; Nazeeruddin, M. K.; Zakeeruddin, S. M.; Tress, W.; Abate, A.; Hagfeldt, A.; Grätzel, M. Cesium-Containing Triple Cation Perovskite Solar Cells: Improved Stability, Reproducibility and High Efficiency. *Energy Environ. Sci.* **2016**, *9* (6), 1989–1997. https://doi.org/10.1039/c5ee03874j.

14. Gao, X. X.; Xue, D. J.; Gao, D.; Han, Q.; Ge, Q. Q.; Ma, J. Y.; Ding, J.; Zhang, W.; Zhang, B.; Feng, Y.; Yu, G.; Hu, J. S. High-Mobility Hydrophobic Conjugated Polymer as Effective Interlayer for Air-Stable Efficient Perovskite Solar Cells. *Sol. RRL* **2019**, *3* (1), 1–8. https://doi.org/10.1002/solr.201800232.

15. Jiang, Q.; Zhao, Y.; Zhang, X.; Yang, X.; Chen, Y.; Chu, Z.; Ye, Q.; Li, X.; Yin, Z.; You, J. Surface Passivation of Perovskite Film for Efficient Solar Cells. *Nat. Photonics* **2019**, *13* (7), 460–466. https://doi.org/10.1038/s41566-019-0398-2.

16. Cheacharoen, R.; Rolston, N.; Harwood, D.; Bush, K. A.; Dauskardt, R. H.; McGehee, M. D. Design and Understanding of Encapsulated Perovskite Solar Cells to Withstand Temperature Cycling. *Energy Environ. Sci.* **2018**, *11* (1), 144–150. https://doi.org/10.1039/c7ee02564e.

17. Dong, D.; Li, J.; Cui, M.; Wang, J.; Zhou, Y.; Luo, L.; Wei, Y.; Ye, L.; Sun, H.; Yao, F. In Situ “Clickable” Zwitterionic Starch-Based Hydrogel for 3D Cell Encapsulation. *ACS Appl. Mater. Interfaces* **2016**, *8* (7), 4442–4455. https://doi.org/10.1021/acsami.5b12141.

18. Acik, M.; Darling, S. B. Graphene in Perovskite Solar Cells: Device Design, Characterization and Implementation. *J. Mater. Chem. A* **2016**, *4* (17), 6185–6235. https://doi.org/10.1039/c5ta09911k.

19. Li, B.; Wang, M.; Subair, R.; Cao, G.; Tian, J. Significant Stability Enhancement of Perovskite Solar Cells by Facile Adhesive Encapsulation. *J. Phys. Chem. C* **2018**, *122* (44), 25260–25267. https://doi.org/10.1021/acs.jpcc.8b09595.

20. Matteocci, F.; Cinà, L.; Lamanna, E.; Cacovich, S.; Divitini, G.; Midgley, P. A.; Ducati, C.; Di Carlo, A. Encapsulation for Long-Term Stability Enhancement of Perovskite Solar Cells. *Nano Energy* **2016**, *30* (July), 162–172. https://doi.org/10.1016/j.nanoen.2016.09.041.

21. Khenkin, M. V.; Katz, E. A.; Abate, A.; Bardizza, G.; Berry, J. J.; Brabec, C.; Brunetti, F.; Bulović, V.; Burlingame, Q.; Di Carlo, A.; Cheacharoen, R.; Cheng, Y. B.; Colsmann, A.; Cros, S.; Domanski, K.; Dusza, M.; Fell, C. J.; Forrest, S. R.; Galagan, Y.; Di Girolamo, D.; Grätzel, M.; Hagfeldt, A.; von Hauff, E.; Hoppe, H.; Kettle, J.; Köbler, H.; Leite, M. S.; Liu, S. (Frank); Loo, Y. L.; Luther, J. M.; Ma, C. Q.; Madsen, M.; Manceau, M.; Matheron, M.; McGehee, M.; Meitzner, R.; Nazeeruddin, M. K.; Nogueira, A. F.; Odabaşı, Ç.; Osherov, A.; Park, N. G.; Reese, M. O.; De Rossi, F.; Saliba, M.; Schubert, U. S.; Snaith, H. J.; Stranks, S. D.; Tress, W.; Troshin, P. A.;

Turkovic, V.; Veenstra, S.; Visoly-Fisher, I.; Walsh, A.; Watson, T.; Xie, H.; Yıldırım, R.; Zakeeruddin, S. M.; Zhu, K.; Lira-Cantu, M. Consensus Statement for Stability Assessment and Reporting for Perovskite Photovoltaics Based on ISOS Procedures. *Nat. Energy* **2020**, *5* (1), 35–49. https://doi.org/10.1038/s41560-019-0529-5.

22. Nair, S.; Gohel, J. V. A Study on Optoelectronic Performance of Perovskite Solar Cell under Different Stress Testing Conditions. *Opt. Mater. (Amst).* **2020**, *109* (August), 110377. https://doi.org/10.1016/j.optmat.2020.110377.

23. Shi, L.; Bucknall, M. P.; Young, T. L.; Zhang, M.; Hu, L.; Bing, J.; Lee, D. S.; Kim, J.; Wu, T.; Takamure, N.; McKenzie, D. R.; Huang, S.; Green, M. A.; Ho-Baillie, A. W. Y. Gas Chromatography-Mass Spectrometry Analyses of Encapsulated Stable Perovskite Solar Cells. *Science (80-.).* **2020**, *368* (6497). https://doi.org/10.1126/science.aba2412.

24. Aranda, C.; Guerrero, A.; Bisquert, J. Crystalline Clear or Not: Beneficial and Harmful Effects of Water in Perovskite Solar Cells. *ChemPhysChem* **2019**, *20* (20), 2587–2599. https://doi.org/10.1002/cphc.201900393.

25. Aristidou, N.; Sanchez-Molina, I.; Chotchuangchutchaval, T.; Brown, M.; Martinez, L.; Rath, T.; Haque, S. A. The Role of Oxygen in the Degradation of Methylammonium Lead Trihalide Perovskite Photoactive Layers. *Angew. Chemie - Int. Ed.* **2015**, *54* (28), 8208–8212. https://doi.org/10.1002/anie.201503153.

26. Senocrate, A.; Acartürk, T.; Kim, G. Y.; Merkle, R.; Starke, U.; Grätzel, M.; Maier, J. Interaction of Oxygen with Halide Perovskites. *J. Mater. Chem. A* **2018**, *6* (23), 10847–10855. https://doi.org/10.1039/c8ta04537b.

27. Agroui, K.; Collins, G. Characterisation of EVA Encapsulant Material by Thermally Stimulated Current Technique. *Sol. Energy Mater. Sol. Cells* **2003**, *80* (1), 33–45. https://doi.org/10.1016/S0927-0248(03)00112-0.

28. Chen, B. M.; Peng, C. Y.; Cho, J. L.; Porter, G. A. Optimization of Solar Module Encapsulant Lamination by Optical Constant Determination of Ethylene-Vinyl Acetate. *Int. J. Photoenergy* **2015**, *2015*. https://doi.org/10.1155/2015/276404.

29. Lang, F.; Gluba, M. A.; Albrecht, S.; Rappich, J.; Korte, L.; Rech, B.; Nickel, N. H. Perovskite Solar Cells with Large-Area CVD-Graphene for Tandem Solar Cells. *J. Phys. Chem. Lett.* **2015**, *6* (14), 2745–2750. https://doi.org/10.1021/acs.jpclett.5b01177.

30. Wang, R.; Xue, J.; Wang, K. L.; Wang, Z. K.; Luo, Y.; Fenning, D.; Xu, G.; Nuryyeva, S.; Huang, T.; Zhao, Y.; Yang, J. L.; Zhu, J.; Wang, M.; Tan, S.; Yavuz, I.; Houk, K. N.; Yang, Y. Constructive Molecular Configurations for Surface-Defect Passivation of Perovskite Photovoltaics. *Science* **2019**, *366* (6472), 1509–1513. https://doi.org/10.1126/science.aay9698.

31. Uddin, A.; Upama, M.; Yi, H.; Duan, L. Encapsulation of Organic and Perovskite Solar Cells: A Review. *Coatings* **2019**, *9* (2), 65. https://doi.org/10.3390/coatings9020065.

32. Bunch, J. S.; Verbridge, S. S.; Alden, J. S.; Van Der Zande, A. M.; Parpia, J. M.; Craighead, H. G.; McEuen, P. L. Impermeable Atomic Membranes from Graphene Sheets. *Nano Lett.* **2008**, *8* (8), 2458–2462. https://doi.org/10.1021/nl801457b.

33. Sheehy, D. E.; Schmalian, J. Optical Transparency of Graphene as Determined by the Fine-Structure Constant. *Phys. Rev. B - Condens. Matter Mater. Phys.* **2009**, *80* (19), 2–5. https://doi.org/10.1103/PhysRevB.80.193411.

34. Cheacharoen, R.; Boyd, C. C.; Burkhard, G. F.; Leijtens, T.; Raiford, J. A.; Bush, K. A.; Bent, S. F.; McGehee, M. D. Encapsulating Perovskite Solar Cells to Withstand Damp Heat and Thermal Cycling. *Sustain. Energy Fuels* **2018**, *2* (11), 2398–2406. https://doi.org/10.1039/c8se00250a.

35. Cheacharoen, R.; Bush, K. A.; Rolston, N.; Harwood, D.; Dauskardt, R. H.; McGehee, M. D. Damp Heat, Temperature Cycling and UV Stress Testing of Encapsulated Perovskite Photovoltaic Cells. In *2018 IEEE 7th World Conference on Photovoltaic Energy Conversion (WCPEC) (A Joint Conference of 45th IEEE PVSC, 28th PVSEC & 34th EU PVSEC)*; IEEE, 2018; pp 3498–3502. https://doi.org/10.1109/PVSC.2018.8547430.

36. You, P.; Liu, Z.; Tai, Q.; Liu, S.; Yan, F. Efficient Semitransparent Perovskite Solar Cells with Graphene Electrodes. *Adv. Mater.* **2015**, *27* (24), 3632–3638. https://doi.org/10.1002/adma.201501145.

37. Kim, G.-H.; Jang, H.; Yoon, Y. J.; Jeong, J.; Park, S. Y.; Walker, B.; Jeon, I.-Y.; Jo, Y.; Yoon, H.; Kim, M.; Baek, J.-B.; Kim, D. S.; Kim, J. Y. Fluorine Functionalized Graphene Nano Platelets for Highly Stable Inverted Perovskite Solar Cells. *Nano Lett.* **2017**, *17* (10), 6385–6390. https://doi.org/10.1021/acs.nanolett.7b03225.

38. Li, H.; Tao, L.; Huang, F.; Sun, Q.; Zhao, X.; Han, J.; Shen, Y.; Wang, M. Enhancing Efficiency of Perovskite Solar Cells via Surface Passivation with Graphene Oxide Interlayer. *ACS Appl. Mater. Interfaces* **2017**, *9* (44), 38967–38976. https://doi.org/10.1021/acsami.7b10773.

39. Yang‡, Q.-D.; Li, J.; Cheng, Y.; Li, H.-W.; Guan, Z.; Yu, B.; Tsang, S.-W. Graphene Oxide as an Efficient Hole-Transporting Material for High-Performance Perovskite Solar Cells with Enhanced Stability. *J. Mater. Chem. A* **2017**, *5* (20), 9852–9858. https://doi.org/10.1039/C7TA01752A.

40. Kim, J. M.; Kim, S.; Choi, S. H. High-Performance n-i-p-Type Perovskite Photodetectors Employing Graphene-Transparent Conductive Electrodes N-Type Doped with Amine Group Molecules. *ACS Sustain. Chem. Eng.* **2019**, *7* (1), 734–739. https://doi.org/10.1021/acssuschemeng.8b04322.

41. Zhu, M.; Liu, W.; Ke, W.; Xie, L.; Dong, P.; Hao, F. Graphene-Modified Tin Dioxide for Efficient Planar Perovskite Solar Cells with Enhanced Electron Extraction and Reduced Hysteresis. *ACS Appl. Mater. Interfaces* **2019**, *11* (1), 666–673. https://doi.org/10.1021/acsami.8b15665.

42. Kim, K.; Lee, Z.; Regan, W.; Kisielowski, C.; Crommie, M. F.; Zettl, A. Grain Boundary Mapping in Polycrystalline Graphene. *ACS Nano* **2011**, *5* (3), 2142–2146. https://doi.org/10.1021/nn1033423.

43. Kim, H. W.; Yoon, H. W.; Yoon, S.; Yoo, B. M.; Ahn, B. K.; Cho, Y. H.; Shin, H. J.; Yang, H.; Paik, U.; Kwon, S. Selective Gas Transport Through Few-Layered Graphene and Graphene

Oxide Membranes. *Science (80-.).* **2013**, *342* (October), 91–95. https://doi.org/10.1126/science.1236098.

44. You, P.; Liu, Z.; Tai, Q.; Liu, S.; Yan, F. Efficient Semitransparent Perovskite Solar Cells with Graphene Electrodes. *Adv. Mater.* **2015**, *27* (24), 3632–3638. https://doi.org/10.1002/adma.201501145.

45. Chen, Y.; Yue, Y.; Wang, S.; Zhang, N.; Feng, J.; Sun, H. Graphene as a Transparent and Conductive Electrode for Organic Optoelectronic Devices. *Adv. Electron. Mater.* **2019**, 1900247. https://doi.org/10.1002/aelm.201900247.

46. Tang, X.; Brandl, M.; May, B.; Levchuk, I.; Hou, Y.; Richter, M.; Chen, H.; Chen, S.; Kahmann, S.; Osvet, A.; Maier, F.; Steinrück, H. P.; Hock, R.; Matt, G. J.; Brabec, C. J. Photoinduced Degradation of Methylammonium Lead Triiodide Perovskite Semiconductors. *J. Mater. Chem. A* **2016**, *4* (41), 15896–15903. https://doi.org/10.1039/c6ta06497c.

47. Zhang, X.; Li, Z.; Ding, Y.; Hu, L.; Ye, J.; Pan, X.; Dai, S. Highly Efficient and Stable Perovskite Solar Cell Prepared from an: In Situ Pre-Wetted PbI2 Nano-Sheet Array Film. *Sustain. Energy Fuels* **2017**, *1* (5), 1056–1064. https://doi.org/10.1039/c7se00080d.

48. Stoumpos, C. C.; Malliakas, C. D.; Kanatzidis, M. G. Semiconducting Tin and Lead Iodide Perovskites with Organic Cations: Phase Transitions, High Mobilities, and near-Infrared Photoluminescent Properties. *Inorg. Chem.* **2013**, *52* (15), 9019–9038. https://doi.org/10.1021/ic401215x.

49. Han, G. H.; Güneş, F.; Bae, J. J.; Kim, E. S.; Chae, S. J.; Shin, H. J.; Choi, J. Y.; Pribat, D.; Lee, Y. H. Influence of Copper Morphology in Forming Nucleation Seeds for Graphene Growth. *Nano Lett.* **2011**, *11* (10), 4144–4148. https://doi.org/10.1021/nl201980p.

50. Zhao, L.; Tian, H.; Silver, S. H.; Kahn, A.; Ren, T. L.; Rand, B. P. Ultrasensitive Heterojunctions of Graphene and 2D Perovskites Reveal Spontaneous Iodide Loss. *Joule* **2018**, *2* (10), 2133–2144. https://doi.org/10.1016/j.joule.2018.07.011.

51. Hoke, E. T.; Slotcavage, D. J.; Dohner, E. R.; Bowring, A. R.; Karunadasa, H. I.; McGehee, M. D. Reversible Photo-Induced Trap Formation in Mixed-Halide Hybrid Perovskites for Photovoltaics. *Chem. Sci.* **2015**, *6* (1), 613–617. https://doi.org/10.1039/c4sc03141e.

52. Lee, J. W.; Kim, D. H.; Kim, H. S.; Seo, S. W.; Cho, S. M.; Park, N. G. Formamidinium and Cesium Hybridization for Photo- and Moisture-Stable Perovskite Solar Cell. *Adv. Energy Mater.* **2015**, *5* (20). https://doi.org/10.1002/aenm.201501310.

53. Calizo, I.; Bejenari, I.; Rahman, M.; Liu, G.; Balandin, A. A. Ultraviolet Raman Microscopy of Single and Multilayer Graphene. *J. Appl. Phys.* **2009**, *106* (4). https://doi.org/10.1063/1.3197065.

54. Brownson, D. A. C.; Banks, C. E. CVD Graphene Electrochemistry: The Role of Graphitic Islands. *Phys. Chem. Chem. Phys.* **2011**, *13* (35), 15825–15828. https://doi.org/10.1039/c1cp21978b.

55. Kasap, S.; Khaksaran, H.; Çelik, S.; Özkaya, H.; Yanik, C.; Kaya, I. I. Controlled Growth of Large Area Multilayer Graphene on Copper by Chemical Vapour Deposition. *Phys. Chem. Chem. Phys.* **2015**, *17* (35), 23081–23087. https://doi.org/10.1039/c5cp01436k.

56. Yoon, T.; Mun, J. H.; Cho, B. J.; Kim, T. S. Penetration and Lateral Diffusion Characteristics of Polycrystalline Graphene Barriers. *Nanoscale* **2014**, *6* (1), 151–156. https://doi.org/10.1039/c3nr03849a.

57. Huang, P. Y.; Ruiz-Vargas, C. S.; Van Der Zande, A. M.; Whitney, W. S.; Levendorf, M. P.; Kevek, J. W.; Garg, S.; Alden, J. S.; Hustedt, C. J.; Zhu, Y.; Park, J.; McEuen, P. L.; Muller, D. A. Grains and Grain Boundaries in Single-Layer Graphene Atomic Patchwork Quilts. *Nature* **2011**, *469* (7330), 389–392. https://doi.org/10.1038/nature09718.

58. Grantab, R.; Shenoy, V. B.; Ruoff, R. S. Anomalous Strength Characteristics of Tilt Grain Boundaries in Graphene. *Science (80-.).* **2010**, *330* (6006), 946–948. https://doi.org/10.1126/science.1196893.

59. Duong, D. L.; Han, G. H.; Lee, S. M.; Gunes, F.; Kim, E. S.; Kim, S. T.; Kim, H.; Ta, Q. H.; So, K. P.; Yoon, S. J.; Chae, S. J.; Jo, Y. W.; Park, M. H.; Chae, S. H.; Lim, S. C.; Choi, J. Y.; Lee, Y. H. Probing Graphene Grain Boundaries with Optical Microscopy. *Nature* **2012**, *490* (7419), 235–239. https://doi.org/10.1038/nature11562.

60. Shahriary, L.; Athawale, A. a. Graphene Oxide Synthesized by Using Modified Hummers Approach. *Int. J. Renew. Energy Environ. Eng.* **2014**, *02* (01), 58–63.

61. Tzeng, P.; Stevens, B.; Devlaming, I.; Grunlan, J. C. Polymer-Graphene Oxide Quadlayer Thin-Film Assemblies with Improved Gas Barrier. *Langmuir* **2015**, *31* (21), 5919–5927. https://doi.org/10.1021/acs.langmuir.5b00717.

62. Liu, H.; Meng, J.; Zhang, X.; Chen, Y.; Yin, Z.; Wang, D.; Wang, Y.; You, J.; Gao, M.; Jin, P. High-Performance Deep Ultraviolet Photodetectors Based on Few-Layer Hexagonal Boron Nitride. *Nanoscale* **2018**, *10* (12), 5559–5565. https://doi.org/10.1039/c7nr09438h.

63. Ramírez, J.; Urbina, A. D.; Kleinschmidt, A. T.; Finn, M.; Edmunds, S. J.; Esparza, G. L.; Lipomi, D. J. Exploring the Limits of Sensitivity for Strain Gauges of Graphene and Hexagonal Boron Nitride Decorated with Metallic Nanoislands. *Nanoscale* **2020**, *12* (20), 11209–11221. https://doi.org/10.1039/d0nr02270e.

Chapter 4. Solid Phase Deposition of Polymeric Hole Transport Layer for Conformal Coating of Monolithic 2-Terminal Perovskite/Silicon Tandem Solar Cells

4.1 Introduction

Silicon photovoltaics have exhibited a substantial decrease in manufacturing costs over the last decade, driven by improved manufacturing techniques and economies of scale.[1] Nevertheless, in the same time period, the power conversion efficiencies of silicon PV have plateaued, as they have approached the theoretical limit for crystalline Si; in order to break through this limit, multi-junction tandem solar cells will be needed.[2] The wide and tunable bandgap of organic-inorganic hybrid perovskites make them an ideal choice for a top cell to couple with a silicon bottom absorber layer.[3] Over the past several years, research on perovskite-silicon tandems has accelerated, with the current record efficiency of 29.8% reported from HZB,[4] exceeding the record 26.6% efficiency currently reported for single-junction Si PV.[5] An ongoing challenge is the fabrication of a uniform perovskite solar cell on top of a silicon solar cell substrate, as the silicon is typically textured with micro-pyramids to increase light trapping.[6] Typical lab-scale thin-film fabrication techniques (e.g. spin-coating) may be unable to yield perovskite films of uniform thickness and morphology when cast atop a non-planar surface,[7] a critical factor for high-performance perovskite devices.[8] This challenge is particularly acute for the application of the charge conduction layers (HTLs and ETLs) which are typically ~10^0–10^1 nm thick,[9] and must be uniformly deposited over areas of ~cm^2 atop micropyramids of ~1-3 μm in height.[10] These constraints have limited most studies to apply the ETL/HTLs via vacuum deposition methods.[11] Nevertheless, film contiguity in vapor deposited films is not always achievable in the ultra-thin (<10 nm) regime.[12] In this paper, we utilize a recently reported method of applying a polymeric film onto textured substrates, called Solid Phase Deposition (SPD), for the deposition of a polymeric HTL.[13] Specifically, pre-deposition of the film solution onto a water bath enables the

generation of a free-standing, solidified HTL film which can be transferred directly onto the textured Si substrate, yielding a conformal coating (Figure 4.1).

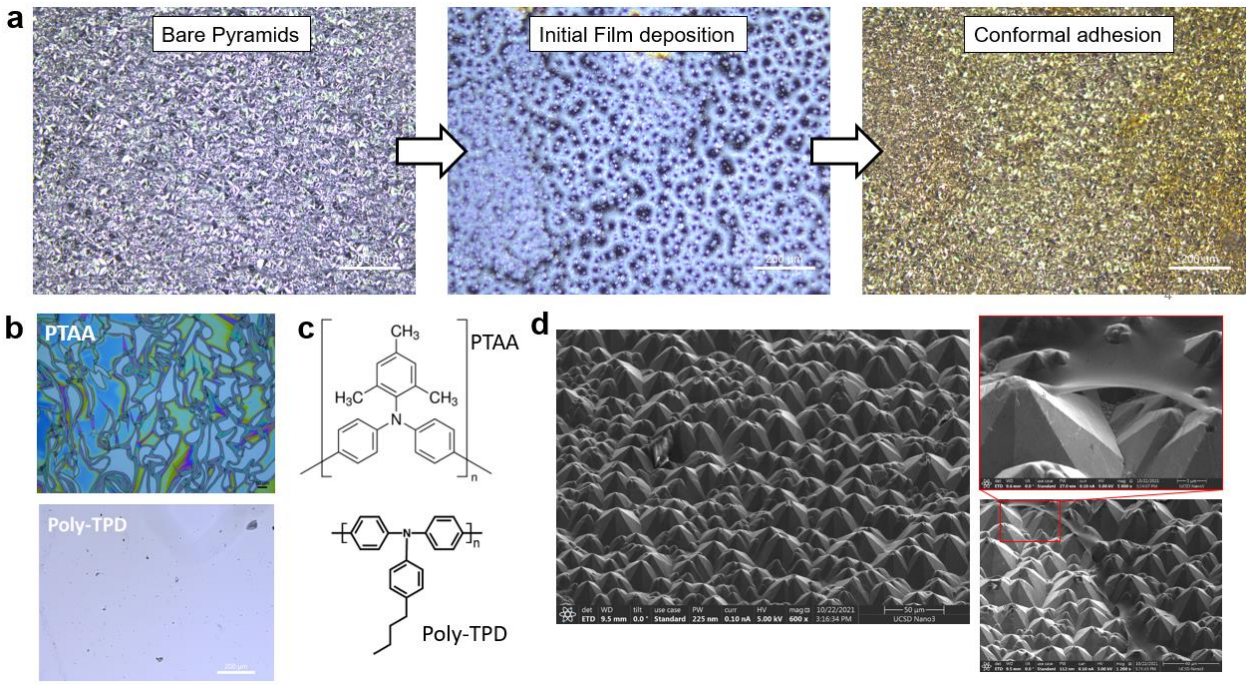

Figure 4.1 Solid Phase Deposition (SPD) of polymeric HTL onto micropyramids. (a) Optical images showing film conforming to substrate, from bare pyramids to initial film deposition to final conformal adhesion. (b) Optical images of two HTL polymer films investigated for this work. (c) Polymeric structures of two HTL polymers investigated: PTAA and poly-TPD. (d) SEM images of coated pyramids, showing fully covered pyramids as well as the boundary between coated and uncoated regions.

Previous research on perovskite/Si tandems has approached the challenge of solution processing onto a textured surface via three broad methods. The first is to remove the top surface texture via polishing, resulting in a flat surface onto which the perovskite top cell can be deposited.[14–16] This method has the advantage of being compatible with existing perovskite solution processing methods, which have been extensively studied in the literature. However, the removal of the textured surface results in a decrease in light trapping, necessitating an application of an anti-reflective coating (ARC)[14] or a textured light management foil (LMF).[15] Furthermore, the increased fabrication cost associated with wafer polishing is generally considered to render this method too expensive for commercialization.[17]

The second approach involves simply flooding the pyramidal valleys with the perovskite absorber until they are fully filled, essentially planarizing the surface. While this method does not require polishing, it does result in two main challenges for perovskite top cell fabrication. The first is that the transport layer beneath the perovskite (the HTL in P-I-N structures or the ETL in N-I-P structures) must still be deposited conformally onto the pyramidal texture.[3] After the HTL/ETL is deposited, the second challenge for researchers is that the perovskite absorber will have wide variations in thickness over its active area, resulting in charge collection anisotropy.[18] Furthermore, such a thick perovskite layer can contribute to substantial parasitic losses in absorption, as well as poor charge extraction in the thicker regions.[19] Some researchers have mitigated these losses by reducing the height of the Si cell pyramids, in some cases decreasing the texturing height down to the nanoscale ("nanopyramids").[20] Indeed, the current record efficiency for perovskite/Si tandems (29.8% PCE from HZB) was achieved using this approach.[21] While shorter pyramids will reduce the thickness variations of subsequent layers, they also decrease the light trapping benefits they were designed for, once again necessitating the addition of an ARC or LMF.[20] We note, however, that neither the ARC/LMF application nor the silicon wafer texturing process is considered prohibitively expensive for commercialization, compared to wafer polishing.[22]

The final approach being used is to apply every layer of the perovskite top cell conformally and uniformly atop the Si texturing (so-called "fully-textured" tandems). This method has several benefits, such as avoiding both polishing and the addition of an ARC/LMF. Furthermore, since all layers are deposited conformally, thicknesses can be optimized for absorbance/charge transport and maintained constant over large areas. The main drawback to this approach is the increased fabrication complexity (though not necessarily cost) of conformally depositing every single layer. Previous studies have predominantly deposited both the HTL and ETL via thermal evaporation.[23] Meanwhile, the perovskite absorber can be deposited by thermal evaporation, electrodeposition, or two-step methods involving thermal evaporation of an inorganic scaffold followed by infiltration

and conversion via solution or vapor. As of publication, the record efficiency for fully textured tandems of 25.2% PCE (Sahli, *et al*) is lower than that of the other two approaches described.[24] This gap can be attributed at least in part due to fewer research efforts having been devoted to these conformal deposition methods compared to solution processing.

Due to high optical absorbance of most high-performance HTL materials in the shorter wavelengths, the P-I-N architecture is currently preferred for monolithic perovskite/Si tandems.[25] Placing this layer beneath the perovskite absorber mitigates the parasitic absorbance of high-energy photons that would occur if it were placed atop the absorber.[26] As a result, of the latter two fabrication methods described previously which could be commercialized affordably, both require a conformal deposition of the HTL onto the textured surface prior to perovskite deposition. The most common approaches of yielding such a conformal coating are thermal evaporation[27] and ALD.[23] Solution processing methods may also be utilized, such as the application of a self-assembled monolayer (SAM),[28] where solution containing unbound material is whisked off the textured substrate. Alternately, Chen, et al, demonstrated a novel approach via a blade coater and nitrogen air blade to deposit their polymer HTL solution and blow away excess material out of the valleys.[29] Processing the HTL via solution, as opposed to via vacuum thermal processing, has the potential to yield several benefits, including lower fabrication costs and faster throughput. In this work we demonstrate the use of a recently-developed solution processed HTL deposition method called Solid Phase Deposition (SPD) for incorporation in a monolithic 2-terminal tandem silicon perovskite solar cell.[13] The HTL material is dissolved in an organic solvent and pre-cast atop a water bath, where the solvent is allowed to dry and a free-floating, solid film remains. The textured silicon bottom solar cell is then stamped directly onto the solid film, which over the course of several minutes conformally adheres to and coats the pyramids. Previous work by our group has demonstrated the utility of this method for numerous polymers over a wide range of moduli and thicknesses.[30] In addition, we have found that the polymer chain alignment resulting from

SPD results in vastly improved hole mobilities compared to other solution processing techniques.[31] By combining SPD of our polymeric HTL with conformal deposition of our perovskite absorber layer, we were able to fabricate conformal perovskite devices on top of micro-pyramid textured monocrystalline silicon solar cells.

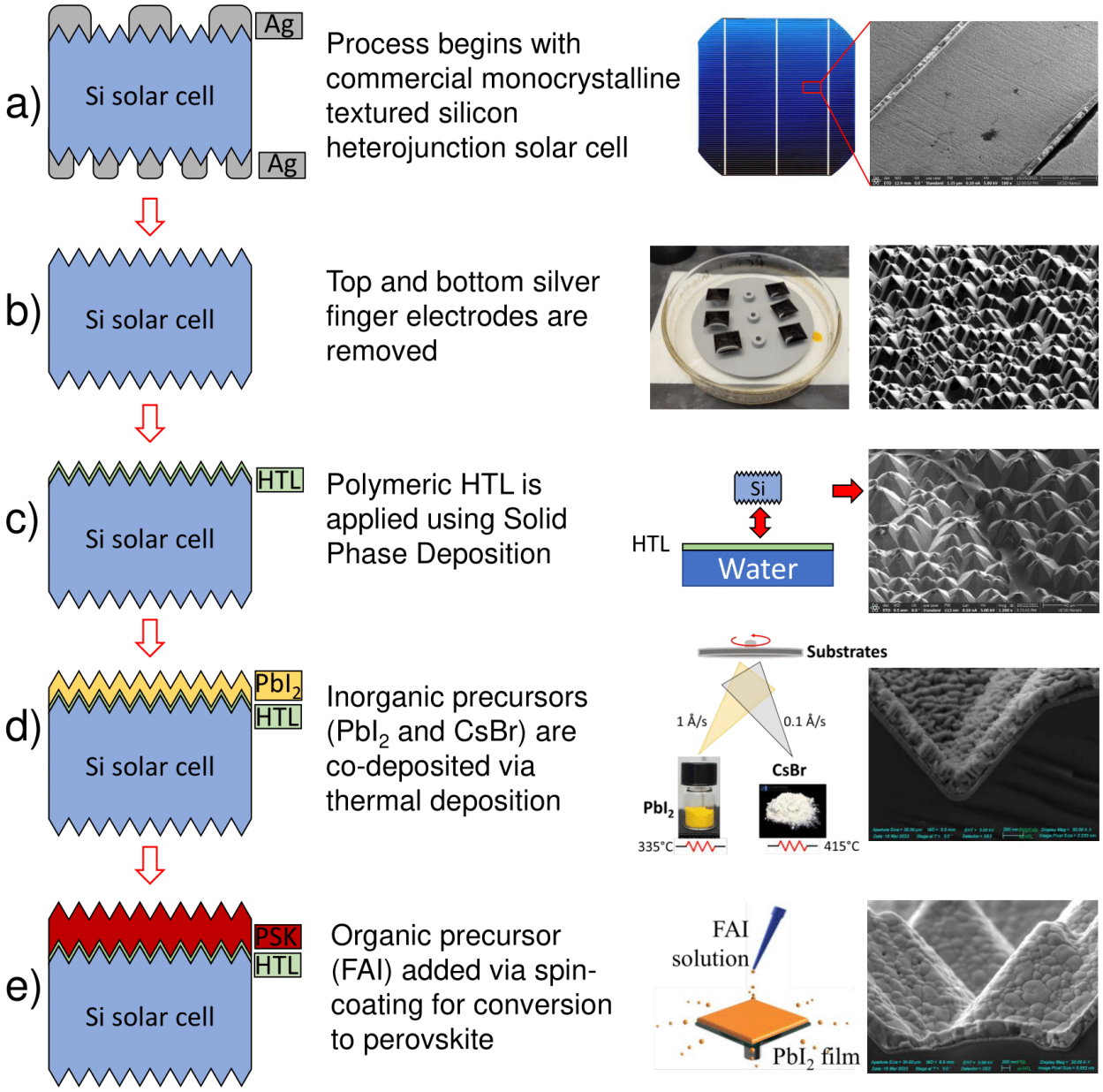

Figure 4.2 Schematic of tandem solar cell fabrication. (a) Process begins with commercial monocrystalline textured silicon heterojunction solar cell. (b) Top and bottom silver finger electrodes are removed. (c) Polymeric HTL is applied using Solid Phase Deposition. (d) Inorganic precursors (PbI_2 and CsBr) are co-deposited via thermal deposition. (e) Organic precursor (FAI) added via spin-coating for conversion to perovskite.

4.2 Materials and Methods

4.2.1 Materials

Front junction single crystal textured bifacial silicon solar cells were obtained from Sunpreme. Perovskite precursors were purchased from Greatcell Solar: formamidinium iodide (FAI), formamidinium bromide (FABr), lead iodide (PbI_2), cesium bromide (CsBr), bathocuproine (BCP), C_{60}. High-temperature thermal evaporation sources were received from Kurt J Lesker: gold shot, silver shot, lithium fluoride, tin oxide, and indium-doped tin oxide (ITO). Polymers were received from ONE Material: poly(4-butyl-N,N-diphenylaniline) (poly-TPD), and poly(triaryl amine) (PTAA). Solvents were obtained from Sigma Aldrich: chlorobenzene (CB), chloroform ($CHCl_3$), and 1,8-diiodooctane (DIO). Aqueous iodine-based silver etchant was purchased from Transene. ITO-coated glass slides were purchased from biotan, with an edge pre-etched for top contacting.

4.2.2 Preparation of Silicon Substrates

Silicon solar cells were received as M2 wafer size (6 in × 6 in) and diced to 11x13 mm (Figure 4.2a). Both the rear and front silver finger electrodes were removed using aqueous iodine etchant (Transene) via immersion overnight (Figure 4.2b). Cells were then rinsed in water and washed in Alconox, acetone, and IPA. Next, 3 mm edge of ITO from the top surface was removed via plasma dry etch (Trion) using CF4 and Ar process gases at an etch rate of 20 nm min^{-1}, for 10 min total. Removal of ITO was confirmed via 4-point probe, and was necessary to prevent internal shorting following deposition of the top cell.

4.2.3 Application of HTL Solution

HTL solution was prepared as follows: poly-TPD polymer (ONE Material) was dissolved in a mixture of CB:$CHCl_3$:DIO (88:11:1) at a concentration of 10 mg mL^{-1}. The solution was allowed to stir for one hour until dissolved, and then filtered successively through filters of pore size 1 µm, 0.45 µm, and 3 × 0.2 µm. Prepared silicon substrates were treated with oxygen plasma

for 5 minutes (300 mTorr base pressure) in order to activate the surface and improve film adhesion. A custom-printed trough was treated with silanes in order to render the surface hydrophobic, and was filled with water right up to the rim. Next, 17 µL of poly-TPD solution was deposited via micropipette over the center of the water trough, which rapidly spread to the edges and dried. Once the film was formed, the silicon substrate was stamped directly onto the surface, with excess polymer removed via tweezers (Figure 4.1 and Figure 4.2c). Conformal coating was confirmed via optical microscope (Leica). Films were allowed to dry briefly in air (< 5 min) before being transferred to a glovebox. The thickness of the HTL layer was 20 nm, measured via Dektak surface profilometry on a control glass slide processed under identical conditions.

4.2.4 Fabrication of Perovskite Absorber

HTL-coated silicon solar cells were loaded into a thermal evaporation chamber into a custom-designed shadow mask. Two Kurt J Lesker Low Temperature Evaporation Sources were installed in the chamber, one containing PbI_2 powder and the other containing CsBr powder. The sources were co-evaporated at 335°C (PbI2) and 415°C (CsBr) yielding deposition rates of 1 Å s^{-1} and 0.1 Å s^{-1} respectively (Figure 4.2d). These rates were confirmed independently during separate calibration runs over a specified time duration, with thickness confirmed via Dektak surface profilometry. The resulting precursor scaffold was measured to be 150 nm thick. Next, FAI solution in ethanol (88 mg mL^{-1}) was spin-coated onto samples in order to yield a perovskite of the following nominal stoichiometry: $(FA_{0.85}Cs_{0.15})Pb(I_{0.95}Br_{0.05})_3$. Dynamic spin coat at 4000 rpm for 30 s in nitrogen environment was used, followed by 15 min anneal at 150°C (Figure 4.2e). Samples were allowed to fully cool before being transferred. The perovskite layer was measured to be 450 nm thick (Dektak). Samples were also prepared on ITO substrates for single junction device characterization. ITO-based devices were completed via thermal evaporation of LiF (1 nm), BCP (10 nm), C_{60} (10 nm) and Ag (100 nm) through a shadow mask.

4.2.5 Device Characterization

Photoluminescence of perovskite films was measured using a fluorescence scope attached to an optical microscope and excited under 514 nm light, and analyzed using OceanView software. UV−vis measurements were taken on a Perkin Elmer LAMBDA 1050+ UV/Vis/NIR spectrophotometer. X-ray diffraction measurements were taken using a Rigaku SmartLab diffractometer. SEM (both top-down and cross-sectional) images were taken using a Zeiss Sigma 500 SEM, with cross-sectional images obtained using a 90° chuck at -5° stage tilt. For solar cell measurements, the current density versus voltage (J−V) characteristics of the cells were measured from −0.1 to 1.0 V using an ABET Sun 2000 solar simulator under an irradiance of 100 mW cm^{-2} from a 150 W Xe short-arc lamp filtered by an AM 1.5G filter. Spectral intensity was calibrated with a silicon reference cell.

4.3 Results and Discussion

4.3.1 Solid Phase Deposition of Polymeric HTL

Common materials for the HTL layer of high-performance perovskite devices include small molecules, such as spiro-OMeTAD, and semiconducting polymers, such as poly(triaryl amine) (PTAA). The SPD process for thin film formation is generally incompatible with small molecules due to the inability for the material to form a cohesive film. Thus, our investigations were limited to polymeric HTL materials only. Among high-performance devices, PTAA is a popular material due to its ideal bandgap and low parasitic absorbance in the shorter wavelength regime. Unfortunately, our PTAA films cast onto water bath were extremely brittle, resulting in numerous tears, folds, and pinholes in the transferred films (Figure 4.1b). This could not be mitigated despite modifications of the solvent mixture or solution temperature, including the addition of plasticizing agents. The side chains of conjugated polymers, in addition to improving solubility with organic solvents, are also known to enhance mechanical deformability due to increased entanglements between chains. With this in mind, we also investigated a structurally similar material to PTAA known as poly-TPD, in which the *para*-methyl group of the central aryl unit has been substituted

with a butyl group (Figure 4.1c). Indeed, this material spread much more uniformly (Figure 4.1b lower), and we could consistently generate films as thin as 20 nm without resulting in pinholes. Furthermore, we confirmed that PTAA and poly-TPD performed comparably to each other when incorporated into full perovskite single-junction devices.

Upon confirmation of contiguous HTL film formation, we then turned our attention to transfer onto the micro-pyramidal silicon substrate. As demonstrated by Esparza, *et al*, certain polymeric materials conform more readily than others; furthermore, film thickness also influences whether full adhesion will occur, vs film "snap-back." Fortunately, as we were working with such thin films, we observed no issue with film adhesion, and films readily adhered under atmospheric conditions to the silicon substrate, as confirmed by optical microscopy (Figure 4.1a). Further confirmation was shown through cross-sectional SEM (Figure 4.1d).

4.3.2 Influence of HTL on Precursor Morphology

On planar substrates, perovskites are typically spin-coated via the solution deposition of all the constituent components from one precursor solution, followed by the rapid addition of an anti-solvent in order to crash out the perovskite crystals and initiate grain formation. On pyramidal substrates, this method would inherently result in flooding of the substrate valleys and poor coverage of the peaks. Thus, a 2-step deposition method is commonly employed in the literature to overcome this challenge, and we acted likewise. First, an inorganic scaffold of PbI_2 and CsBr was co-evaporated via vacuum thermal deposition. The CsBr was included in order to stabilize the final perovskite chemistry; at room temperature, formamidinium lead iodide ($FAPbI_3$) is inherently unstable and reverts from its black, light-absorbing alpha phase to the yellow, photo-inactive delta phase. The inclusion of cesium stabilizes the structure and inhibits the phase transition from occurring.

Interestingly, we observed an unusual morphology of this scaffold layer, as shown in SEM image Figure 4.3d. Specifically, we observed what was termed a “feather-like” morphology, with highly porous structure with grains fanning out from the substrate. Such a morphology is ideal for a 2-step conversion as it offer a high surface area for infiltration of the organic precursors during the subsequent conversion reaction.

Intriguingly, this morphology was only observed on our pyramidal substrates coated with HTL via SPD. We note that the pyramidal silicon solar cells have a ~100 nm thick coating of ITO deposited on the surface to act as both a current collector and an anti-reflective layer. When the scaffold layer was deposited onto planar ITO substrates that had been coated with poly-TPD via spin-coating, a more dense morphology was observed. Even more interestingly, we observed the continuation of the feather-like structure in some regions of our solar cells where the poly-TPD film did not conformally adhere to the pyramids (incomplete HTL coating was a phenomenon observed in our earlier trials while the stamping procedure was still being optimized). Previous work by our group has shown how the deposition method of conjugated polymers has a strong influence on film morphology, texture, and polymer chain orientation. Thus, we conclude that the surface texture of the poly-TPD film generated from the SPD process, in combination with the energetics of the ITO top electrode, act in tandem to preferentially nucleate PbI_2 crystals in this outward orientation throughout large areas of the film.

4.3.3 Comparison of Perovskite Conversion Methods

The conversion step of the perovskite layer synthesis involved the addition of our organic precursor FAI, in order to generate $FAPbI_3$ perovskite; more accurately, the nominal stoichiometry of our absorber layers was $(FA_{0.85}Cs_{0.15})Pb(I_{0.95}Br_{0.05})_3$, due to the inclusion of CsBr during the co-evaporation process. For this conversion reaction, we investigated two different methods. The first was a spin-coat conversion, wherein the PbI_2 scaffold acts as a sponge, absorbing the needed solution for a stoichiometric reaction. Excess solution is ejected from the substrate at a

high spin speed. This method has been previously reported in the literature, and a highly porous scaffold is needed to ensure adequate organic precursor penetration. The second method was the use of chemical vapor deposition (CVD) using a vacuum tube furnace. By controlling the source and substrate temperatures, both the vapor flux of FAI and the deposition and substrate conversion kinetics could be controlled. In both cases, a conformal perovskite layer was generated, and the resulting film morphologies and optoelectronic behaviors were examined in detail.

As shown in Figure 4.3a, the spin-coat converted film exhibited markedly higher photoluminescence than the tube furnace CVD film. Despite films looking similar after conversion (a dark red color), it was challenging to detect any PL activity from the CVD films. In contrast, both UV-vis and XRD showed minimal differences between the two types of films. Indeed, Tauc plots for the two types of films (Figure 4.3b) show nearly identical bandgaps of 1.5 eV. This similarity can be further noted in the films' x-ray diffractograms (Figure 4.3c), which show a clear elimination of the PbI_2 precursor peak at 12° for both types of perovskite films. We note that full conversion via CVD was not always achieved, and was highly sensitive to film placement within the tube furnace. Nevertheless, in all films showing full conversion via XRD and identical bandgaps via UV-vis, the large difference in PL remained. The cause of this discrepancy was revealed in film analysis via cross-sectional SEM. As shown in Figures 4.3e-f, CVD films resulted in a more porous, discontinuous, and less dense morphology than spin-coated films. These discontinuities can inhibit charge transport, and serve as recombination sites that diminish PL and charge extraction.

Based on these observations, the spin coat conversion method was determined to be the preferred approach for perovskite synthesis.

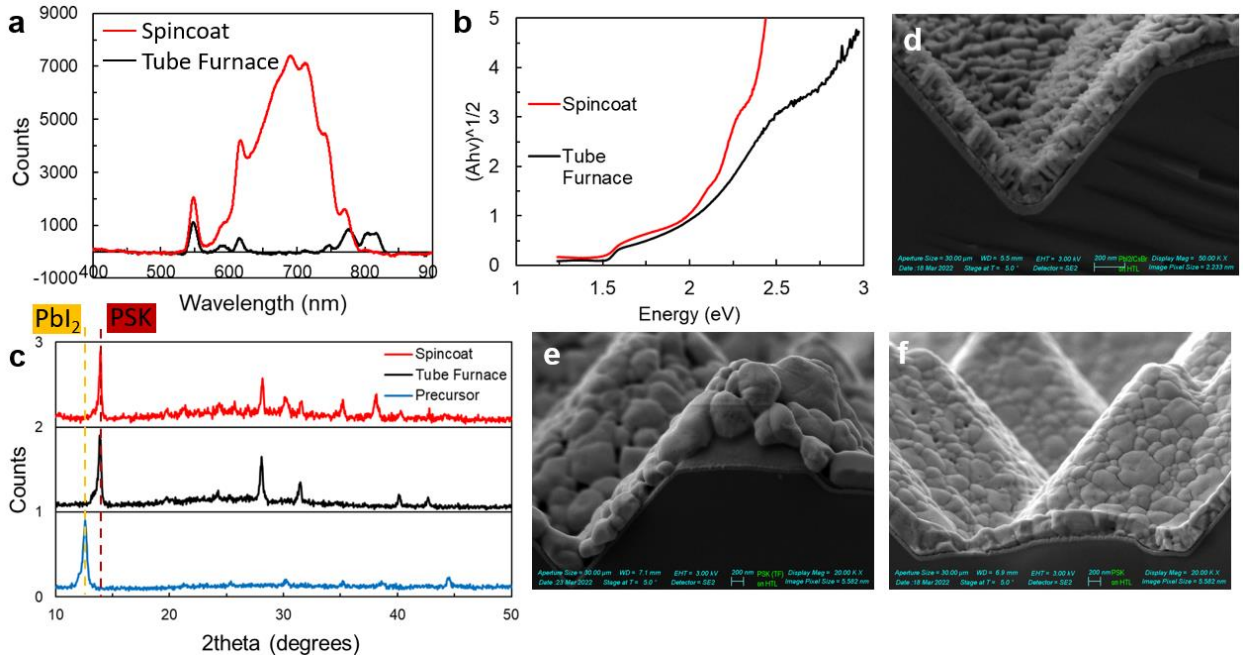

Figure 4.3 Comparison of spin coating and CVD for perovskite conversion. (a) Photoluminescence spectra, (b) Tauc plots, and (c) X-ray diffractograms of perovskite films. (d-f) Cross-sectional SEM micrographs of (d) PbI2 scaffold, (e) CVD perovskite, and (f) spin coated perovskite.

4.3.4 Solar Cell Performance

When fabricating a tandem perovskite/silicon solar cell, it is required for the upper perovskite solar cell two transparent electrodes, so as to allow longer-wavelength light to pass through the top cell and into the bottom silicon layer. Typically, a transparent conducting oxide (TCO) such as ITO or IZO is used. In our commercial silicon cells from Sunpreme, a charge collection layer of ITO is already present, acting as a recombination junction in the middle of the device. As of publication, however, the procedure is still being developed for depositing a top-layer TCO, as well as a SnOx buffer layer needed to prevent damage during ITO deposition. As a result, in order to probe the efficacy of our fabrication procedure, we prepared planar solar cells on transparent ITO/glass substrates alongside our textured devices. This allowed us to deposit a

non-transparent silver anode on top via previously established methods. The performance metrics for these devices is shown in Figure 4.4. Current-voltage (*J*-V) sweeps are shown for spin-converted perovskite on spin-coated HTL (a), spin-converted perovskite on SPD HTL (b), and CVD-converted perovskite on SPD HTL (c). The device performance metrics (V_{oc}, J_{sc}, FF, and PCE) are given in in (d), (e), (f) and (g), respectively. Unsurprisingly, the spin-converted samples out-performed our CVD converted devices, with a champion performance of 6.5% vs to 1.0% PCE. We again attribute this to poor grain formation within the CVD films, resulting in poor charge extraction and high recombination losses. We did observe higher performance in our spin-coated HTL devices, although we attribute this mainly to the presence of inhomogeneities in our SPD films. Such asperities were not observed in the textured substrates and would not be of concern in our tandem devices. Overall, this device performance represents a promising first step towards optimizing the device fabrication procedure, with the ultimate goal of testing device performance of a fully integrated tandem perovskite/silicon device.

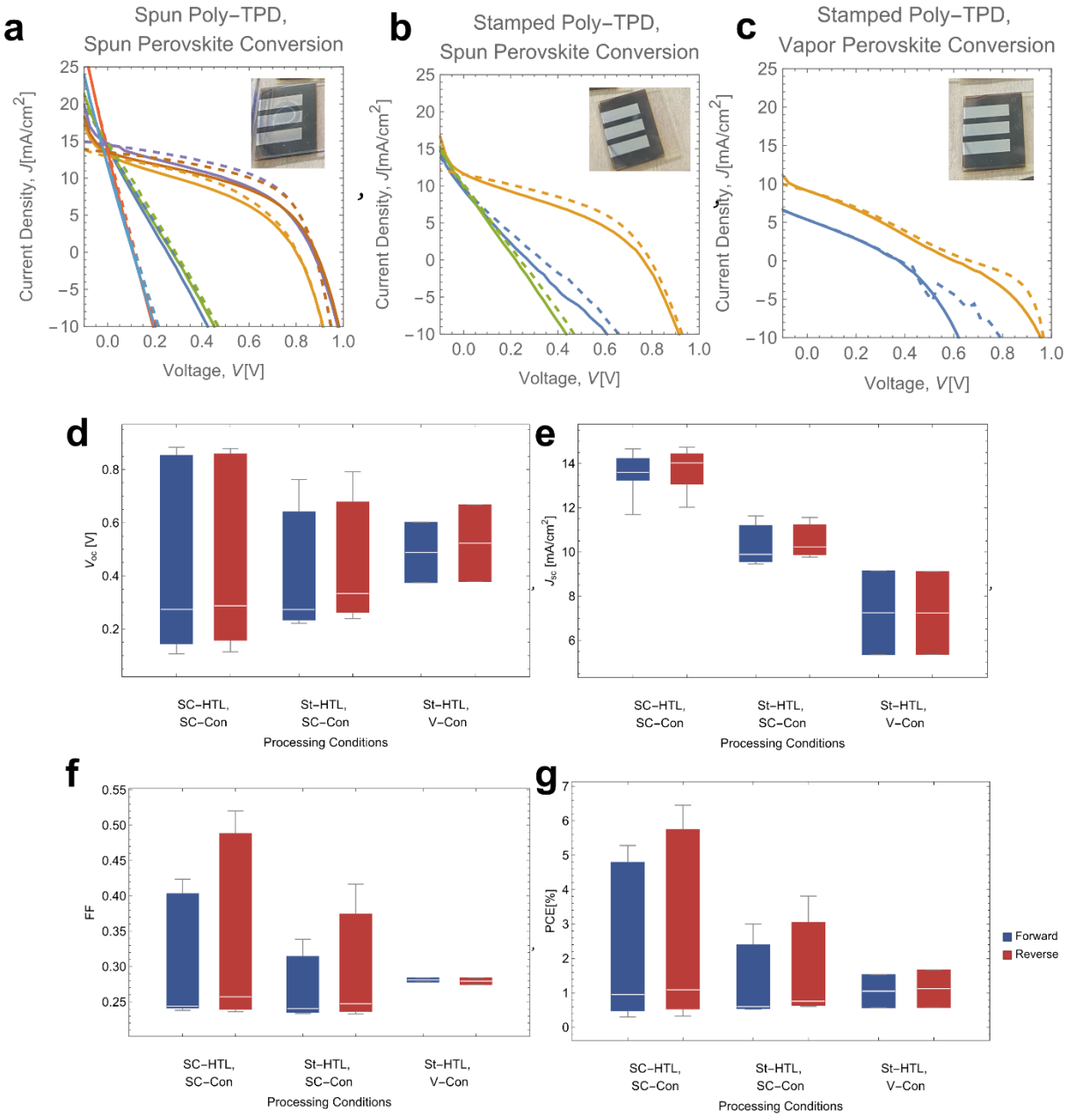

Figure 4.4 Solar cell performance for perovskite devices. (a-c) Current-Density (*J*-V) curves for spin-coat HTL/spin-coat perovskite (a), stamped HTL/spin-coat perovskite (b), and stamped HTL/CVD perovskite (c). (d-g) Device performance metrics for our devices, showing V_{oc} (d), J_{sc} (e), fill factor (f), and power conversion efficiency (g).

4.4 Conclusions

We applied a new polymer coating technique–Solid Phase Deposition–for the conformal deposition of polymeric hole transport layers onto textured micropyramids of silicon solar cells.

Experimental results show high degrees of film compliance with the substrates, with 20nm thick films fully adhering to the surface of 3 μm tall pyramids without ripping or tearing. The texture of the polymer film has additional benefits for the subsequent deposition of perovskite absorber layers, as it preferentially nucleates inorganic lead iodide crystals into a highly porous “feather-like” orientation, compared to a more compact crystal structure formed on spin-coated HTL films. This feather-like morphology is desirable for organic precursor infiltration, and results in a compact perovskite film with large crystal size. In fabricating our FAPbI3 perovskite films, we investigated two conversion methods, namely spin coating and tube furnace chemical vapor deposition. While both achieved full conversion, the spin coated films exhibited markedly higher photoluminescence due to larger grain boundaries, and also resulted in higher-performing solar cells. Future work in this area will confirm these findings on textured cells upon completion of the device architecture, and will hopefully represent a promising step forward towards the commercialization of fully textured monolithic two-terminal tandem perovskite on silicon photovoltaics.

Chapter 4, in full, is a reprint of the material “Solid Phase Deposition of Polymeric Hole Transport Layer for Conformal Coating of Monolithic 2-Terminal Perovskite/Silicon Tandem Solar Cells” which is currently under preparation for submission, by Runser, R., Esparza, G., Cramlet, J., Gupta, A., Kodur, M., Chen, A.X., Simon, I., Fenning, D.P., and Lipomi, D.J. The dissertation author was the first author of this paper, all authors contributed to this work.

4.5 References

1. Shen, H.; Walter, D.; Wu, Y.; Fong, K. C.; Jacobs, D. A.; Duong, T.; Peng, J.; Weber, K.; White, T. P.; Catchpole, K. R. Monolithic Perovskite/Si Tandem Solar Cells: Pathways to Over 30% Efficiency. *Adv. Energy Mater.* **2020**, *10* (13), 1–18. https://doi.org/10.1002/aenm.201902840.

2. Barkhouse, D. A. R.; Gunawan, O.; Gokmen, T.; Todorov, T. K.; Mitzi, D. B. Yield Predictions for Photovoltaic Power Plants:Empirical Validation,Recent Advances and Remaining Uncertainties. *Prog. Photovoltaics Res. Appl.* **2015**, *20* (1), 6–11. https://doi.org/10.1002/pip.

3. Werner, J.; Niesen, B.; Ballif, C. Perovskite/Silicon Tandem Solar Cells: Marriage of Convenience or True Love Story? – An Overview. *Adv. Mater. Interfaces* **2018**, *5* (1), 1–19. https://doi.org/10.1002/admi.201700731.

4. Al-Ashouri, A.; Köhnen, E.; Li, B.; Magomedov, A.; Hempel, H.; Caprioglio, P.; Márquez, J. A.; Vilches, A. B. M.; Kasparavicius, E.; Smith, J. A.; Phung, N.; Menzel, D.; Grischek, M.; Kegelmann, L.; Skroblin, D.; Gollwitzer, C.; Malinauskas, T.; Jošt, M.; Matič, G.; Rech, B.; Schlatmann, R.; Topič, M.; Korte, L.; Abate, A.; Stannowski, B.; Neher, D.; Stolterfoht, M.; Unold, T.; Getautis, V.; Albrecht, S. Monolithic Perovskite/Silicon Tandem Solar Cell with >29% Efficiency by Enhanced Hole Extraction. *Science (80-.).* **2020**, *370* (6522), 1300–1309. https://doi.org/10.1126/SCIENCE.ABD4016/SUPPL_FILE/ABD4016_AL-ASHOURI_SM.PDF.

5. Yoshikawa, K.; Yoshida, W.; Irie, T.; Kawasaki, H.; Konishi, K.; Ishibashi, H.; Asatani, T.; Adachi, D.; Kanematsu, M.; Uzu, H.; Yamamoto, K. Exceeding Conversion Efficiency of 26% by Heterojunction Interdigitated Back Contact Solar Cell with Thin Film Si Technology. *Sol. Energy Mater. Sol. Cells* **2017**, *173* (June), 37–42. https://doi.org/10.1016/j.solmat.2017.06.024.

6. Manzoor, S.; Filipič, M.; Onno, A.; Topič, M.; Holman, Z. C. Visualizing Light Trapping within Textured Silicon Solar Cells. *J. Appl. Phys.* **2020**, *127* (6). https://doi.org/10.1063/1.5131173.

7. Bornside, D. E. Mechanism for the Local Planarization of Microscopically Rough Surfaces by Drying Thin Films of Spin-Coated Polymer/Solvent Solutions. *J. Electrochem. Soc.* **1990**, *137* (8), 2589–2595. https://doi.org/10.1149/1.2086992.

8. Du, T.; Xu, W.; Xu, S.; Ratnasingham, S. R.; Lin, C. T.; Kim, J.; Briscoe, J.; McLachlan, M. A.; Durrant, J. R. Light-Intensity and Thickness Dependent Efficiency of Planar Perovskite Solar Cells: Charge Recombinationversusextraction. *J. Mater. Chem. C* **2020**, *8* (36), 12648–12655. https://doi.org/10.1039/d0tc03390a.

9. Kim, G. W.; Shinde, D. V.; Park, T. Thickness of the Hole Transport Layer in Perovskite Solar Cells: Performance versus Reproducibility. *RSC Adv.* **2015**, *5* (120), 99356–99360. https://doi.org/10.1039/c5ra18648j.

10. Basu, P. K.; Khanna, A.; Hameiri, Z. The Effect of Front Pyramid Heights on the Efficiency of Homogeneously Textured Inline-Diffused Screen-Printed Monocrystalline Silicon Wafer Solar Cells. *Renew. Energy* **2015**, *78*, 590–598. https://doi.org/10.1016/j.renene.2015.01.058.

11. Jošt, M.; Kegelmann, L.; Korte, L.; Albrecht, S. Monolithic Perovskite Tandem Solar Cells : A Review of the Present Status and Advanced Characterization Methods Toward 30 % Efficiency. **2020**. https://doi.org/10.1002/aenm.201904102.

12. Ramírez, J.; Polat, B.; Lipomi, D. J. Metallic Nanoislands on Graphene for Biomechanical Sensing. *ACS Omega* **2020**, *5* (26), 15763–15770. https://doi.org/10.1021/acsomega.0c01967.

13. Esparza, G. L.; Lipomi, D. J. Solid-Phase Deposition: Conformal Coverage of Micron-Scale Relief Structures with Stretchable Semiconducting Polymers. *ACS Mater. Lett.* **2021**, *3*, 988–995. https://doi.org/10.1021/acsmaterialslett.1c00213.

14. Chen, B.; Yu, Z.; Liu, K.; Zheng, X.; Liu, Y.; Shi, J.; Spronk, D.; Rudd, P. N.; Holman, Z.; Huang, J. Grain Engineering for Perovskite/Silicon Monolithic Tandem Solar Cells with Efficiency of 25.4%. *Joule* **2019**, *3* (1), 177–190. https://doi.org/10.1016/j.joule.2018.10.003.

15. Bush, K. A.; Manzoor, S.; Frohna, K.; Yu, Z. J.; Raiford, J. A.; Palmstrom, A. F.; Wang, H. P.; Prasanna, R.; Bent, S. F.; Holman, Z. C.; McGehee, M. D. Minimizing Current and Voltage Losses to Reach 25% Efficient Monolithic Two-Terminal Perovskite-Silicon Tandem Solar Cells. *ACS Energy Lett.* **2018**, *3* (9), 2173–2180. https://doi.org/10.1021/acsenergylett.8b01201.

16. Jošt, M.; Köhnen, E.; Morales-Vilches, A. B.; Lipovšek, B.; Jäger, K.; Macco, B.; Al-Ashouri, A.; Krč, J.; Korte, L.; Rech, B.; Schlatmann, R.; Topič, M.; Stannowski, B.; Albrecht, S. Textured Interfaces in Monolithic Perovskite/Silicon Tandem Solar Cells: Advanced Light Management for Improved Efficiency and Energy Yield. *Energy Environ. Sci.* **2018**, *11* (12), 3511–3523. https://doi.org/10.1039/c8ee02469c.

17. Zhengshan J. Yu, Brian M. Wheelwright, S. M. & Z. C. H. Silicon Wafers with Optically Specular Surfaces Formed by Chemical Polishing. *J. Mater. Sci. Mater. Electron.* **2016**, *27*, 10270–10275.

18. Akhil, S.; Akash, S.; Pasha, A.; Kulkarni, B.; Jalalah, M.; Alsaiari, M.; Harraz, F. A.; Balakrishna, R. G. Materials & Design Review on Perovskite Silicon Tandem Solar Cells : Status and Prospects 2T , 3T and 4T for Real World Conditions. *Mater. Des.* **2021**, *211*, 110138. https://doi.org/10.1016/j.matdes.2021.110138.

19. Bi, D.; Tress, W.; Dar, M. I.; Gao, P.; Luo, J.; Renevier, C.; Schenk, K.; Abate, A.; Giordano, F.; Correa Baena, J. P.; Decoppet, J. D.; Zakeeruddin, S. M.; Nazeeruddin, M. K.; Grätzel, M.; Hagfeldt, A. Efficient Luminescent Solar Cells Based on Tailored Mixed-Cation Perovskites. *Sci. Adv.* **2016**, *2* (1). https://doi.org/10.1126/sciadv.1501170.

20. Jäger, K.; Sutter, J.; Hammerschmidt, M.; Schneider, P. I.; Becker, C. Prospects of Light Management in Perovskite/Silicon Tandem Solar Cells. *Nanophotonics* **2021**, *10* (8), 1991–2000. https://doi.org/10.1515/nanoph-2020-0674.

21. Becker, C.; Albrecht, S.; Stannowski, B. World record again at HZB: Almost 30 % efficiency for next-generation tandem solar cells https://www.helmholtz-berlin.de/pubbin/news_seite?nid=23248;sprache=en.

22. Iqbal, S.; Zhang, L. J.; Fu, X. C.; Su, D.; Zhou, H. L.; Wu, W.; Zhang, T. Highly-Efficient Low Cost Anisotropic Wet Etching of Silicon Wafers for Solar Cells Application. *AIP Adv.* **2018**, *8* (2). https://doi.org/10.1063/1.5012125.

23. Jošt, M.; Bertram, T.; Koushik, D.; Marquez, J. A.; Verheijen, M. A.; Heinemann, M. D.; Köhnen, E.; Al-Ashouri, A.; Braunger, S.; Lang, F.; Rech, B.; Unold, T.; Creatore, M.; Lauermann, I.; Kaufmann, C. A.; Schlatmann, R.; Albrecht, S. 21.6%-Efficient Monolithic Perovskite/Cu(In,Ga)Se 2 Tandem Solar Cells with Thin Conformal Hole Transport Layers for Integration on Rough Bottom Cell Surfaces. *ACS Energy Lett.* **2019**, *4* (2), 583–590. https://doi.org/10.1021/acsenergylett.9b00135.

24. Sahli, F.; Werner, J.; Kamino, B. A.; Bräuninger, M.; Monnard, R.; Paviet-Salomon, B.; Barraud, L.; Ding, L.; Diaz Leon, J. J.; Sacchetto, D.; Cattaneo, G.; Despeisse, M.; Boccard, M.;

Nicolay, S.; Jeangros, Q.; Niesen, B.; Ballif, C. Fully Textured Monolithic Perovskite/Silicon Tandem Solar Cells with 25.2% Power Conversion Efficiency. *Nat. Mater.* **2018**, *17* (9), 820–826. https://doi.org/10.1038/s41563-018-0115-4.

25. Taghavi, M. J.; Houshmand, M.; Zandi, M. H.; Gorji, N. E. Modeling of Optical Losses in Perovskite Solar Cells. *Superlattices Microstruct.* **2016**, *97*, 424–428. https://doi.org/10.1016/j.spmi.2016.06.031.

26. Jiang, Y.; Almansouri, I.; Huang, S.; Young, T.; Li, Y.; Peng, Y.; Hou, Q.; Spiccia, L.; Bach, U.; Cheng, Y. B.; Green, M. A.; Ho-Baillie, A. Optical Analysis of Perovskite/Silicon Tandem Solar Cells. *J. Mater. Chem. C* **2016**, *4* (24), 5679–5689. https://doi.org/10.1039/c6tc01276k.

27. Löper, P.; Moon, S. J.; Martín De Nicolas, S.; Niesen, B.; Ledinsky, M.; Nicolay, S.; Bailat, J.; Yum, J. H.; De Wolf, S.; Ballif, C. Organic-Inorganic Halide Perovskite/Crystalline Silicon Four-Terminal Tandem Solar Cells. *Phys. Chem. Chem. Phys.* **2015**, *17* (3), 1619–1629. https://doi.org/10.1039/c4cp03788j.

28. Al-Ashouri, A.; Köhnen, E.; Li, B.; Magomedov, A.; Hempel, H.; Caprioglio, P.; Márquez, J. A.; Vilches, A. B. M.; Kasparavicius, E.; Smith, J. A.; Phung, N.; Menzel, D.; Grischek, M.; Kegelmann, L.; Skroblin, D.; Gollwitzer, C.; Malinauskas, T.; Jošt, M.; Matič, G.; Rech, B.; Schlatmann, R.; Topič, M.; Korte, L.; Abate, A.; Stannowski, B.; Neher, D.; Stolterfoht, M.; Unold, T.; Getautis, V.; Albrecht, S. Monolithic Perovskite/Silicon Tandem Solar Cell with >29% Efficiency by Enhanced Hole Extraction. *Science (80-.).* **2020**, *370* (6522), 1300–1309. https://doi.org/10.1126/science.abd4016.

29. Chen, B.; Yu, Z. J.; Manzoor, S.; Wang, S.; Weigand, W.; Yu, Z.; Yang, G.; Ni, Z.; Dai, X.; Holman, Z. C.; Huang, J. Blade-Coated Perovskites on Textured Silicon for 26%-Efficient Monolithic Perovskite/Silicon Tandem Solar Cells. *Joule* **2020**, *4* (4), 850–864. https://doi.org/10.1016/j.joule.2020.01.008.

30. Runser, R.; Root, S. E.; Ober, D. E.; Choudhary, K.; Chen, A. X.; Dhong, C.; Urbina, A. D.; Lipomi, D. J. Interfacial Drawing: Roll-to-Roll Coating of Semiconducting Polymer and Barrier Films onto Plastic Foils and Textiles. *Chem. Mater.* **2019**, *31* (21), 9078–9086. https://doi.org/10.1021/acs.chemmater.9b03343.

31. Choudhary, K.; Chen, A. X.; Pitch, G. M.; Runser, R.; Urbina, A.; Dunn, T. J.; Kodur, M.; Kleinschmidt, A. T.; Wang, B. G.; Bunch, J. A.; Fenning, D. P.; Ayzner, A. L.; Lipomi, D. J. Comparison of the Mechanical Properties of a Conjugated Polymer Deposited Using Spin Coating, Interfacial Spreading, Solution Shearing, and Spray Coating. *ACS Appl. Mater. Interfaces* **2021**, *13* (43), 51436–51446. https://doi.org/10.1021/acsami.1c13043.

Chapter 5. Conclusions and Future Perspectives

5.1 Interfacial Drawing

The first project in this dissertation presents a novel method for fabricating large-area polymer thin films called Interfacial Drawing. The polymer of choice is dissolved in an organic solvent and cast atop a water bath, where it spontaneously spreads and dries to form a solid, free-standing thin film. By continuously injecting solution on one end of the trough, while continuously rolling and transferring the opposite solid end onto a substrate, a continuous roll-to-roll process can be achieved. This chapter described in detail the process parameters that influenced film thickness, showing how it could be carefully tuned to yield films between 10-80nm thick. In addition, we investigated the mechanical properties of the resulting films, and discovered that they exhibited a lower modulus and greater fracture strain than films prepared via spin coating. These properties are desirable for flexible applications, an area for which semiconducting polymers are especially applicable. Finally, we demonstrated the utility of Interfacial Drawing to the fabrication of organic electronic devices, namely flexible organic solar cells, showing their performance again compared to spin coating devices.

This research offers numerous avenues for potential future investigations. While the trough used for this study was limited to a width of 4 inches due to geometrical constrains, an expansion to 6 inches (along with investigation of methods to delay or eliminate the observed process termination) would allow for use with wafers and substrates more commonly used in photovoltaic processing. Additional investigations into a broader array of substrates can also be undertaken. Textiles and fabrics, whose porosity makes them challenging to coat with uniform films via traditional solution processing techniques, are an ideal candidate. For example, fabric-mounted solar cells could be produced for use in collapsible power generation or indoor Internet-of-Things applications. Finally, further studies can be undertaken into the enhanced mechanical

properties of films produced via Interfacial Drawing, particularly applications of their improved deformability and the mechanism of film formation underlying this finding.

5.2 Graphene Barriers

The second project in this dissertation investigates the utility of graphene barriers for encapsulating perovskite solar cells. Graphene is known to be impermeable to small species ingress; nevertheless, numerous grain boundaries within a graphene film can offer pathways through which moisture and oxygen can travel. Stacking multiple layers of graphene can block access to those pathways, improving the film's barrier metrics. We therefore investigated the performance of single- and multi-layer graphene against a control barrier of Parylene-C, the polymer support layer present in all of the films. Surprisingly, we found a remarkable improvement in barrier performance upon the addition of a single layer of graphene, followed by minimal subsequent improvements in 2- and 3-layer graphene. This finding suggests that mechanically staked multilayer graphene offers substantial lateral material transport pathways, thus negating any proposed benefit offered from multilayer graphene. Furthermore, given that each additional layer confers a 3% decrease in optical transmissivity, the single-layer graphene was found to be the optimal material among the barrier films tested.

5.3 Perovskite Silicon Tandem Solar Cells

The final chapter of this dissertation discusses the fabrication of fully textured monolithic 2-terminal perovskite silicon solar cells. A novel process called Solid Phase Deposition (SPD) was recently demonstrated for its ability to conformally coat polymer thin films onto micropyramids of anisotropic etched silicon. Similar to Interfacial Drawing, but via a batch-scale process, a polymer solution is cast atop a water bath and allowed to spread and dry into a free-floating solid film. The film can then be stamped with a microtextured substrate, and given the correct range of elastic moduli and film thicknesses, the film will spontaneously deform to adhere to the pyramid surfaces. In my work, we began with commercial silicon cells, which are themselves microtextured

to enhance light trapping, and coated them with a conjugated polymer hole transport layer via SPD. We subsequently deposited a perovskite light-absorbing layer via a two-step process. First an inorganic lead iodide scaffold was deposited via thermal evaporation. Then, two methods were investigated for the conversion reaction to a perovskite upon the addition of an organic precursor: chemical vapor deposition (CVD) and spincoating. While both methods could fully react and convert the lead iodide, the spin coat approach yielded much larger grains and consequently a stronger photoluminescent output. The approach was validated via fabrication of planar solar cells, which similarly exhibited better performance (higher power conversion efficiency) when fabricated via spin-coating vs CVD.

Future work on this project first should focus on the conformal deposition of the electron transport layer and transparent conducting oxide top contacts. These straightforward steps will enable validation of the tandem architecture and allow for layer thickness and interface optimization. In the longer term, silicon perovskite tandem cells offer one of the most promising research avenues for exceeding the theoretical efficiency limit of single-junction solar cells. Silicon photovoltaics are already a well-established technology with reliable power output, dependable lifetimes, and plummeting costs; meanwhile, perovskite solar cells are being intensively researched, with performance metrics continuing to improve, and raw materials being abundant and inexpensive. At the moment, fully textured perovskite silicon tandems are challenging to research due to the difficulty of fabricating each layer of the perovskite top cell uniformly over the silicon micropyramids. It is hoped that this work, and other research on conformal thin-film deposition, can contribute to ongoing efficiency gains among multiple emerging photovoltaic technologies.